Structural Basis of Unidirectional Export of Lipopolysaccharide to the Cell Surface

Published in final edited form as:

Nature. 2019 March ; 567(7749): 550–553. doi:10.1038/s41586-019-1039-0.

Structural basis for unidirectional export of lipopolysaccharide to the cell surface

Tristan W. Owens[1], **Rebecca J. Taylor**[1,*], **Karanbir Pahil**[1,*], **Blake Bertani**[2,*], **Natividad Ruiz**[2], **Andrew C. Kruse**[3], and **Daniel Kahne**[1,3,†]

[(1)]Department of Chemistry and Chemical Biology, Harvard University, Cambridge, MA, 02138, USA

[(2)]Department of Microbiology, The Ohio State University, Columbus, OH, 43210 USA

[(3)]Department of Biological Chemistry and Molecular Pharmacology, Harvard Medical School, Boston, MA, 02115, USA

Gram-negative bacteria are surrounded both by an inner cytoplasmic membrane and by an outer membrane that serves as a protective barrier to limit entry of many antibiotics. The distinctive properties of the outer membrane are due to the presence of lipopolysaccharide[1]. This large glycolipid with numerous sugars is made in the cytoplasm and a complex of proteins forms a membrane-to-membrane bridge that mediates transport from the inner membrane to the cell surface[1]. The inner membrane components of the protein bridge comprise an ATP-binding cassette (ABC) transporter that powers transport, but how this transporter ensures unidirectional lipopolysaccharide movement across the bridge to the outer membrane is mysterious[2]. Here we describe two crystal structures of a five-component inner membrane complex that contains all the proteins required to extract lipopolysaccharide from the membrane and pass it to the protein bridge. These structures, combined with biochemical and genetic experiments, identify the path for lipopolysaccharide entry into the cavity of the transporter and up to the bridge. We also identify a protein gate that must open to allow movement of substrate from the cavity onto the bridge. Lipopolysaccharide entry into the cavity is ATP-independent, but ATP is required for lipopolysaccharide movement past the gate and onto the bridge. Our findings explain how the inner membrane transport complex controls efficient unidirectional transport of lipopolysaccharide against its concentration gradient.

Correspondence to: Natividad Ruiz; Andrew C. Kruse.

[†]Correspondence and requests for materials should be addressed to kahne@chemistry.harvard.edu.

Author contributions:

DK and TWO conceptualized the project. TWO performed crystallographic experiments; TWO and ACK solved and refined the structures. TWO, RJT, and KP performed biochemical experiments that BB, NR and DK helped conceptualize. BB performed *in vivo* functional assays conceptualized by BB and NR. TWO, RJT, KP, and DK wrote the manuscript; all authors contributed to editing.

[*]These authors contributed equally to this work

The authors declare no competing interests.

Data Availability:

Coordinates and structure factors have been deposited in the Protein Data Bank under accession numbers 6MIT for the *E. cloacae* $LptB_2FGC$ and 6MJP for the *V. cholerae* $LptB_2FGC$ structure.

Lipopolysaccharide (LPS) biosynthesis is completed in the outer leaflet of the inner membrane. LPS is then transported to the outer membrane by a protein bridge comprising seven conserved lipopolysaccharide transport proteins ($LptB_2FGCADE$, Fig. 1a)[3,4]. The inner membrane components, $LptB_2FG$, comprise an ABC transporter[5–7], a family of proteins conserved in all domains of life[8,9]. ATP binding and hydrolysis by the cytoplasmic ATPase LptB provides the energy to move LPS across the periplasmic bridge[10,11]. $LptB_2FG$ forms a stable sub-complex with another component, LptC, which is anchored in the membrane by a single transmembrane (TM) helix[5,12]. LptC receives LPS from LptFG and transfers it to LptA[4,10], which connects the inner membrane complex to LptDE, the outer membrane translocon[4,13–17]. The bridge model for LPS transport has been likened to a PEZ candy dispenser in which candies are pushed up the stack and out of the dispenser by a spring at the base[2,4]. $LptB_2FG$ serves as the spring, but there is no molecular understanding of how this complex functions to achieve unidirectional LPS transport.

LptC, which contains a periplasmic domain that binds LPS[10,18], is the key to understanding unidirectional movement of LPS. The recent structures of $LptB_2FG$[19,20] did not define the path taken by LPS during movement into the cavity and out of the membrane. We screened homologs of $LptB_2FGC$ from multiple Gram-negative bacteria for functional protein expression (Extended Data Fig. 1), and obtained crystals of *Vibrio cholerae* and *Enterobacter cloacae* $LptB_2FGC$ complexes that were refined to 2.85 Å and 3.2 Å resolution, respectively (Fig. 1b, Extended Data Fig. 2, and Supplementary Data Table 1).

LptF and LptC form a continuous β-jellyroll via an edge-to-edge interaction between their C- and N-terminal β-strands (Fig. 1b), and there are numerous contacts between side chains on the convex surfaces of the LptF and LptG β-jellyroll sheets. The transmembrane anchor of LptC interdigitates between LptG TM1 and LptF TM5 (Figs. 1b and c). No other ABC-system contains a transmembrane helix from another protein incorporated directly into the transporter[9,21]. Below we show that this helix regulates transport activity.

To probe the *in vivo* relevance of the crystal structures, we incorporated a photocrosslinkable unnatural amino acid (*p*-benzoylphenylalanine, *p*BPA) at multiple sites in LptFGC[22] and probed protein-protein contacts. We replaced several residues at the interface between LptC and LptF, and at the terminal β-strand of the LptG β-jellyroll (Fig. 2a). We found extensive crosslinks between LptC and LptF, but the only crosslink between LptC and LptG was from a residue on the convex side of LptC that faces LptG (Fig. 2b, Extended Data Fig. 4a). We conclude that the marked asymmetry observed in the crystal structure is physiologically relevant.

LptC creates a single pathway for entry and movement of LPS onto the bridge. Although LptC mutants lacking the TM helix can survive in the laboratory, only full length LptC is found in the wild, implying a strong selection for the TM helix[23,24]. To probe the role of the LptC TM helix, we compared the functions of $LptB_2FG$ complexes containing either no LptC, wild-type LptC or LptC with the TM helix removed (hereafter ΔTM-LptC) in proteoliposomes. LPS transport to LptA was greatly diminished in the absence of LptC, but ΔTM-LptC, which stably associated with $LptB_2FG$ (Extended Data Fig. 4b), supported transport comparably to full-length LptC (Fig. 2c). However, even when a large excess

(10X) of ΔTM-LptC was used, the ATPase activity of the ΔTM-LptC complex was substantially higher than for $LptB_2FGC$[4] (Fig. 2d; Extended Data Fig. 4c). Because $LptB_2FGC$ containing full length LptC uses less ATP to transport LPS than $LptB_2FG$ with ΔTM-LptC, we conclude that the TM domain of LptC modulates ATP hydrolysis to achieve more efficient coupling of ATP hydrolysis and LPS movement.

Previous structures of $LptB_2FG$ suggested an alternating-access model with two possible gates on opposite sides of the transporter for entry of LPS into the cavity (Fig. 2e, left panel, and Extended Data Fig. 5)[19,20]. In the absence of LptC, these entry paths are structurally similar and related by two-fold rotational pseudosymmetry. However, the presence of the LptC TM helix breaks the symmetry and differentiates the potential points of entry. Our structures define a single path for LPS entry into the cavity between LptG TM1 and LptF TM5 where the TM segment of LptC is located; this path is directly aligned with the concave surface of the continuous β-jellyroll formed by the interaction LptF and LptC. Entry between LptG TM5 and LptF TM1 is prevented by the steric barrier created by the convex surface of the continuous LptC-LptF β-jellyroll (Fig. 2e, right panel).

To probe how LPS moves into the cavity and up to LptC, we used *in vivo* photocrosslinking to determine where LPS binds.[10] We trapped LPS in two distinct regions of the transporter (Fig. 3 and Extended Data Figs. 6 and 7): at the base of the transport machine between the interdigitated LptC helix and LptG TM1 and LptF TM5 (Fig. 3a and b, and Extended Data Fig 6c and d) and at the interface of the β-jellyroll between LptF and LptC (Fig. 3c, Extended Fig. 7). We did not observe crosslinks to LPS at the alternate entry point between LptG TM5 and LptF TM1 (Extended Data Fig. 6e). The crosslinks at the base of the transporter report on how LPS enters the cavity and we trapped LPS at two sites, one located just outside the cavity as defined by crosslinks to LptC(M19*p*BPA) and LptF(S315*p*BPA), and one located inside the cavity as defined by LptC(G21*p*BPA) and LptG(S30*p*BPA). The crosslinks at the interface between the β-jellyrolls of LptF and LptC (LptC(F78*p*BPA) and LptF(R223*p*BPA), Fig. 3b,c and Extended Data Fig. 6a) report on how LPS moves from the cavity onto the bridge, and are also consistent with the single path for movement defined by the structures.

We compared *in vivo* crosslinking intensities at the different LPS binding sites (Fig. 3b in wild-type and catalytically dead complexes to probe which steps in LPS transport are ATP-dependent. Crosslinking was negligible to the β-jellyroll of LptC and LptF in the complex that contained the inactive LptB(E163Q)[11] ATPase, but was much stronger to binding sites at the base of the cavity. In contrast, the LPS crosslinks to the β-jellyroll of LptC and LptF were much stronger in complexes containing wild-type LptB. These results suggested that entry into the cavity of the $LptB_2FGC$ transporter does not require ATP hydrolysis, but accumulation of LPS in the β-jellyroll does. Increased crosslinking intensities at the base of the cavity for the inactive transporter likely reflects the build-up of LPS in the inner membrane due to impaired transport.[12]

We performed *in vitro* crosslinking experiments to clarify whether entry into the cavity or extraction from the membrane requires ATP. Crosslinking to LPS at residue LptC(G21*p*BPA), at the base facing the interior of the cavity, was observed in the absence of

ATP (resting state) and in a pre-hydrolysis state where ATP is present but hydrolysis is not possible due to a lack of Mg^{2+} (+ EDTA, Fig. 3d). Crosslinking to LptC(F78*p*BPA) in the β-jellyroll was not observed under these conditions. Similar results were obtained for the complex containing the E163Q mutant or when the non-hydrolyzable ATP analog AMPPNP was used (Extended Data Fig. 6c). Weak crosslinking to LptC(F78*p*BPA) was observed in the presence of ATP and vanadate (Fig 3d), consistent with a transporter that can extract but cannot turn over continually due to inhibition by ADP-vanadate. Taken together, these results show that entry into the transporter cavity does not require ATP; however, ATP is required to extract LPS out of the membrane.

The LPS transporter presents a problem not found in other ABC transporter systems because LPS in the bridge can potentially flow backward when the cavity reopens. Unless the rate of entry of LPS into the cavity is much faster than backward flow, there must be a mechanism to prevent the latter or transport would be inefficient. A notable feature of our $LptB_2FGC$ crystal structures is that the β-jellyroll of LptF exists in two structurally distinct states: in the *E. cloacae* complex it is open (Fig. 4a and b), but in the *V. cholerae* complex it is closed (Fig. 4b, Extended Data Fig. 8). To determine if transport requires access to the open state, we introduced a pair of cysteines capable of forming a disulfide bond into LptF to trap it in the closed state (Fig. 4c). Cells expressing LptF containing each single cysteine mutant were viable, but those producing the double cysteine variant, LptF(Cys2), were not although cellular levels were similar to wild-type LptF (Extended Data Fig. 9a–c). LptF(Cys2) was dominant negative, implying that the mutant LptF formed a non-functional complex with the other inner membrane Lpt components (Extended Data Fig. 9d). We successfully purified $LptB_2F$(Cys2)GC complexes (Extended Data Fig. 9e), showing that the loss of viability was not due to an assembly defect. Using an *in vitro* LPS transport assay (Fig. 4d), we observed transport by the Cys2 mutant complex only upon the addition of DTT (Fig. 4e), which reduced the disulfide and allowed LptF to access an open state. In contrast, ATP hydrolysis occurred regardless of whether the gate in LptF was open or closed (Extended Data Fig. 9f), indicating that gate-opening is not directly coupled to ATP hydrolysis. We infer that movement of the substrate, driven by ATP binding or hydrolysis, pushes the gate open. Spontaneous gate closure behind the substrate provides a mechanism to reduce the rate of backward flow when the cavity opens again.

Based on the structural and functional studies reported here, we propose the following model for LPS transport. First, newly synthesized LPS present in the inner membrane binds at the entry point defined by the LptC TM segment intercalated between LptG TM1 and LptF TM5 (Fig 4f), and ATP-independent entry of LPS into the cavity past the LptC TM segment occurs[25]. ATP-dependent cavity constriction then provides the force to push LPS out of the membrane. The LptC TM helix coordinates ATP hydrolysis with extraction from the membrane, and this role in transport efficiency apparently provides such an important fitness advantage that it is conserved in the wild even though it can be bypassed in the laboratory under certain conditions.[23,26] The gate in the β-jellyroll of LptF also improves transport efficiency by preventing backward movement of LPS into the membrane as the cavity reopens, ensuring unidirectional traffic from LptC to LptA and through LptDE to the outer membrane.

As proper LPS transport is critical for survival, the structures and functional information reported here may lead to new strategies for the development of antibiotics. Such strategies may include binding tightly to LPS in the cavity of the machine to jam it or disrupting interfaces between components of the machine to reduce efficiency of transport. Compounds that impair outer membrane assembly would make Gram-negative bacteria sensitive to many antibiotics that cannot normally penetrate.

Methods

Cloning, expression, and purification of $LptB_2FGC$ homologs

Genes encoding LptB, LptC, and LptFG were PCR amplified from *Enterobacter cloacae subsp. cloacae* ATCC 13047 and *Vibrio cholerae* C6706 genomic DNA. LptB and LptFG PCR products were inserted into pCDFduet by Gibson assembly (New England Biolabs) to generate plasmids analogous to those previously used for the *E. coli* homologs[10]. LptC PCR products were subcloned into pET22/42 and then inserted into pBADHisA, with a C-terminal thrombin cleavage site and hepta-histidine tag. Oligonucleotides primers were purchased from IDT or Eton Biosciences, and are listed in Supplementary Table 1. Plasmids pBADHisA-LptC-thrombin-his_7 and pCDFduet-LptB-LptFG were then co-transformed into C43 *E. coli*.

For overexpression of *E. cloacae* $LptB_2FGC$-his_7 complexes, overnight cultures of C43 *E. coli* containing pBADHisA-LptC-thrombin-his_7 and pCDFduet-LptB-LptFG were diluted 1:100 into M9 minimal media (Cold Spring Harbor) supplemented with trace elements, 50 μg/mL carbenicillin, and 50 μg/mL spectinomycin. These cultures were grown at 37 °C, 200 rpm to OD_{600} = 1.0, then cooled to 30 °C, and induced by addition of 200 μM isopropyl-β-D-thiogalactoside (IPTG) and 0.02% L-arabinose. After 12 h expression, cells were harvested by centrifugation and resuspended in buffer containing 20 mM Tris-HCl (pH=7.4), 300 mM NaCl, 0.2 mM ethylenediaminetetraacetic acid (EDTA), 1 mM phenylmethylsulfonyl fluoride (PMSF), and supplemented with 100 μg/mL lysozyme, 50 μg/mL DNAse I, and cOmplete protease inhibitor tablets (Sigma). Resuspended cells were lysed by a 3x passage through an Emulsiflex C3 homogenizer (Avestin) at 15,000 psi. Unbroken cells were removed from the lysate by centrifugation at 12,000 x g, 4 °C for 10 minutes, and then membranes were pelleted by ultracentrifugation at 100,000 x g, 4 °C for 1 h in a Beckman 45Ti rotor. Membrane pellets were resuspended in solubilization buffer (20 mM Tris (pH=7.4), 300 mM NaCl, 10% v/v glycerol, 5 mM $MgCl_2$, cOmplete protease inhibitor), homogenized using an IKA T18 basic UltraTurrax, supplemented with 1% w/v n-dodecyl β-D-maltoside (DDM; Anatrace)and 2 mM adensosine 3'-triphosphate (ATP), and then rocked at 4 °C for 2 h. Insoluble cell debris were removed by ultracentrifugation 100,000 x g, 4 °C for 30 min and the clarified, solubilized membranes rocked with Ni-NTA agarose (Qiagen) in a gravity flow column for 2 h. Following incubation and flow-through, the resin was washed with 20 column volumes (cv) of wash buffer (20 mM Tris pH7.4, 300 mM NaCl, 10% glycerol, 0.05% DDM) containing 20 mM imidazole, then 30 cv of wash buffer containing 35 mM imidazole. Protein was eluted with 4 cv of wash buffer containing 200 mM imidazole. The protein was then concentrated using an Amicon 100-kDa molecular weight cutoff centrifugation filter (EMD Millipore). Concentrated eluate was applied to a

Superdex 200 Increase 10/300 gel filtration column (GE Healthcare) equilibrated in 300 mM NaCl, 20 mM Tris (pH =7.4), 5% v/v glycerol 0.025 % w/v DDM (Anatrace), 0.5 mM tris(3-hydroxypropyl)phosphine (THP; EMD Millipore). Peak fractions were combined, incubated overnight at 4 °C with restriction grade thrombin (EMD Millipore) to cleave the hepta-histidine tag. After tag cleavage, the sample was supplemented with 8 mM imidazole, flowed twice through Ni-NTA resin equilibrated with gel filtration buffer and 8 mM imidazole, then concentrated to 10–15 mg/mL using a 100-kDa cut-off concentrator (Millipore) for crystallization or use in biochemical assays.

V. cholerae $LptB_2FGC$ was expressed and purified in the same manner as the *E. cloacae* $LptB_2FGC$, with slight modifications. Overnight expression in C43 *E. coli* was carried out in Luria broth at 20 °C (LB, Miller) rather than M9 media at 30 °C. The lysis buffer contained 20 mM Tris-HCl (pH = 8.0), 300 mM NaCl, 0.2 mM EDTA, and 1mM PMSF. The Ni-NTA wash buffer contained 300 mM NaCl, 20 mM Tris (pH = 8.0), 10% glycerol, and 0.1% DDM. The gel filtration buffer contained 0.05% w/v DDM and 0.1% w/v CYMAL-6 (Anatrace), 3% v/v glycerol, 300 mM NaCl, 20 mM Tris (pH = 8.0), and 0.5 mM THP.

To generate inactive variants of $LptB_2FGC\text{-}his_7$ complexes, site-directed mutagenesis was used to introduce a glutamate to glutamine substitution at LptB-E163 in pCDFduet-LptB-LptFG. LptB-E163 is strictly conserved in all known homologs of LptB[11], and is the catalytic base which deprotonates water for nucleophilic attack on the terminal phosphate of ATP, a mechanism conserved in all ABC-systems[8]. Purification of $LptB(E163Q)_2FGC\text{-}his_7$ complexes was carried out in the same manner as the corresponding wild-type complexes, except that ATP was spiked into the Ni-NTA eluate to a final concentration of 2 mM prior to the first concentration step.

Crystallization of $LptB_2FGC$

Wild-type *E. cloacae* $LptB_2FGC$ was crystallized by the vapor diffusion method in hanging drops at 4 °C. Protein samples with the tag cleaved were concentrated to 14 mg/ml, supplemented with 2 mM Na-novobiocin, and mixed at a 2:1 protein : precipitant ratio with a precipitant solution consisting of 500 mM Li_2SO_4, 100 mM MES (pH = 6.5), and 21% v/v PEG400. We had previously shown novobiocin binds to *E. coli* $LptB_2FGC$ and solved a co-crystal structure of LptB alone bound to novobiocin[27], and so thought that it might stabilize a conformation of the full complex. In sparse-matrix screening with *E. cloacae* $LptB_2FGC$ we found several conditions which were dependent on the presence of Na-novobiocin in the protein sample. In this form, however, novobiocin is not bound in a functionally significant site but is instead involved forming crystal contacts (see below). Streak-seeding into freshly set drops significantly improved crystal morphology. Crystals grew to full size within three weeks and were then dehydrated by increasing the concentration of PEG 400 in the reservoir by 2% per day up to 35% v/v PEG 400. Crystals were frozen directly from drops or briefly cryoprotected in a solution containing 500 mM NaCl, 2 mM Na-novobiocin, 100 mM MES (pH = 6.5), and 35% v/v PEG400 before being flash-frozen and stored in liquid nitrogen.

Inactive *V. cholerae* $LptB(E163Q)_2FGC$ was crystallized by vapor diffusion in sitting drops at 4 °C. Protein samples were concentrated to 16 mg/ml, supplemented with 5 mM Na-ATP and 2 mM EDTA, and mixed at a 2:1 protein : precipitant ratio with a precipitant solution

consisting of 200 mM $CaCl_2$, 100 mM Tris-HCl (pH = 8.5), and 40% v/v PEG400. Crystals appeared after 1 – 2 weeks and grew to full size within 6 weeks. Crystals could be obtained from these conditions without ATP in the sample or in earlier purification steps, however crystals obtained in this way were much lower quality. Likewise, crystals of similar morphology could also be obtained using wild-type $LptB_2FGC$ and the non-hydrolysable ATP analog, AMPPNP. Crystals could be harvested directly from drops and flash frozen in liquid nitrogen, but addition to the drop of ~10 μL of a cryo-solution containing 41% v/v PEG400, 200 mM $CaCl_2$, 300 mM NaCl, and 100 mM Tris-HCl (pH = 8.5) was often necessary to facilitate freezing of long, fragile plates.

Data collection and structure determination

Diffraction data were collected at Argonne National Laboratory beamline GM/CA 23-ID-D at wavelength 1.033 Å for *E. cloacae* $LptB_2FGC$ crystals, and NE-CAT beamline 24-ID-E at 0.979 Å for *V. cholerae* $LptB(E163Q)_2FGC$ crystals. Data were integrated in XDS[28] and scaled in the CCP4[29] suite program AIMLESS[30]. Molecular replacement for the *E. cloacae* data was performed in Phaser[31] using the transmembrane domains of *K. pneumoniae* $LptB_2FG$ (PDB ID 5L75)[19], two copies of *E. coli* LptB (PDB ID 6B89)[27] and one copy of *E. coli* LptC (PDB ID 3MY2)[18]. After one round of refinement in Phenix[32], transmembrane helix of LptC as well as most of the periplasmic domains of LptF and LptG were built manually in Coot[33] using 5L75 and 5X5Y to guide assignment of amino acid identity. At that point it became clear the LptC periplasmic domain was misplaced by Phaser, with register of the strands in the β-jellyroll being off by one full strand, as LptC residues 1–57 were not present in either of the previously solved structures (3MY2 and 4B54) but residues 42–57 comprise the β-strand at the interface between LptC and LptF. Nonetheless in this structure, LptC residues 25–38 could not be resolved. Further model building and refinement were carried out alternately in Coot and phenix.refine[34]. Non-crystallographic symmetry restraints were used early in refinement to constrain the two copies of $LptB_2FGC$ in the asymmetric unit but were not used between the two copies of LptB with each complex. The final model contained 94.45%, 5.47%, and 0.08% in the favored, allowed, and outlier regions of the Ramachandran plot, respectively.

Given the dependence of crystal formation on the presence of novobiocin in the protein sample, we had hoped to see it bound at the interface between LptB and LptFG, as observed in our previous work (see PDB IDs 6B89, 6B8B, ref. 4). There was no unexplained electron density near either copy of residue LptB(F90), but one novobiocin molecule could be accommodated at the interface between the two non-crystallographically symmetric copies of $LptB_2FGC$ (Extended Data Fig. 10a) and thereby explain the dependence of crystallization on novobiocin.

The structure of *V. cholerae* $LptB(E163Q)_2FGC$ was determined by molecular replacement using the *E. cloacae* structure as a search model. Significantly different conformations of the periplasmic domains of LptF, LptG, and LptC required manual rebuilding of these regions. In the structure, the residues connecting the transmembrane helix of LptC to the periplasmic β-jellyroll domain were fully resolved, although a few loops between transmembrane helices of LptF and LptG remained disordered. No density corresponding to bound nucleotides

could be observed. Density likely corresponding to bound detergent molecules and ordered PEGs could be found surrounding the transmembrane helices and nucleotide binding domains, respectively (Extended Data Fig. 10b,c). We further observed large, unexplained areas of electron density in the lumen between the transmembrane helices (Extended Data Fig. 10d,e). Some of this could correspond to bound detergent or PEG molecules; however, the size, continuity, and distance from the protein suggest that this electron density more likely corresponds to low-occupancy or partially disordered LPS molecules that co-purified with the $LptB_2FGC$ complex (Extended Data Fig. 10d,e). The final refined model contained 95.64%, 4.36%, and 0.0% in the favored, allowed, and outlier regions of the Ramachandran plot, respectively.

In vivo photocrosslinking experiments

To search for interactions between $LptB_2FGC$ components, as well as between Lpt proteins and LPS, *in vivo* photocrosslinking experiments were performed as described previously[10], with minor modifications. BL21(DE3) *E. coli* strains were transformed with pSup-BpaRS-6TRN[22], pBADHisA-LptC-thrombin-His_7, and pCDFduet-LptB(WT or E163Q)-LptFG, with amber (TAG) codons introduced at one position in either LptF, LptG, or LptC. 50 mL cultures of these strains were grown at 37 °C in LB containing 50 μg/mL spectinomycin, 50 μg/mL carbenicillin, 30 μg/mL chloramphenicol, and 0.7 mM *p*-benzoylphenylalanine (pBPA; BaChem). When the cultures reached OD_{600} ~ 0.8, expression of pBPA-substituted $LptB_2FGC$ complexes was induced by addition of 20 μM IPTG and 0.02% L-arabinose. After 2 h expression at 37 °C, cultures were divided into UV- and UV+ samples, the former set aside, and the later exposed to UV light (λ=365 nm) at room temperature for 5 min.

To facilitate western blot analysis of Lpt-Lpt and Lpt-LPS adducts, pBPA substituted $LptB_2FGC$-his complexes were solubilized and purified by nickel affinity chromatography. First, cells from both UV- and UV+ samples were pelleted by centrifugation (5,000 *g*, 10 min, 4 °C), resuspended in 2mL buffer A (20mM Tris (pH=8.0), 300 mM NaCl, 15 mM imidazole, 5 mM $MgCl_2$, 1% w/v Anzergent 3–14 (Anatrace), and 1 mM PMSF) containing 100 μg/mL lysozyme, and 50 μg/mL DNAseI, and then disrupted by 3 freeze-thaw cycles alternating between liquid nitrogen and an ice water bath. After the third freeze-thaw cycle, samples were incubated on ice for 30 min, at which point they had turned from cloudy to clear, and insoluble cell debris were removed by centrifugation for 30 min at 18,500 *g*. Solubilized supernatants were then applied to Ni-NTA resin (250 μL resin per sample) pre-equilibrated with buffer A. After flow-through the resin was washed once with 1 mL buffer A and twice with 5 mL of wash buffer containing 20 mM Tris (pH=8.0), 300 mM NaCl, 0.1% w/v Anzergent 3–14, and 20 mM imidazole. His-tagged $LptB_2FGC$ complexes were eluted with 2 × 750 μL wash buffer containing 200 mM imidazole. To concentrate the samples, proteins were precipitated from the eluate by addition of 10% w/v trichloroaceticacid (TCA), incubated on ice 30 min, pelleted at 21,500 *g* for 30 min at 4 °C; following, the supernatant was aspirated off and pellets rinsed with 500μL cold acetone, and then pelleted again 21,500 *g* for 30 min at 4 °C. Finally, the acetone was aspirated off, and the protein pellet resuspended in 80 μL SDS gel loading buffer.

For western blot analysis, these samples were boiled, separated by SDS-PAGE, and transferred to PVDF membranes (Bio-Rad). Detection of protein bands was achieved by labeling with rabbit antisera against LptF[23], LptG[23], LptC[35] followed by donkey anti-rabbit HRP conjugate secondary antibody (GE Amersham), or by mouse anti-His_5 HRP conjugate (Qiagen). Lpt-LPS adducts were detected by anti-LPS core mouse monoclonal antibody – HRP conjugate (Hycult Biotechnology). Bands were visualized using ECL™ Prime Western Blotting Detection Reagent (GE Amersham), and imaged using an Azure c600 (Azure Biosystems).

Reconstitution of LPS release to LptA by *E. cloacae* and *V. cholerae* $LptB_2FGC$ complexes.

Genes encoding LptA homologs were PCR amplified from *V. cholerae* and *E. cloacae* genomic DNA and incorporated into pET22b in a manner that replaced the native signal sequences with the plasmid-encoded pelB leader and added a His_6 tag to the C-terminus. Amber mutations for pBPA incorporation were made at positions which aligned with *E. coli* LptA(I36) (Extended Data Fig. 3) to generate *V. cholerae* pET22b-pelBss-LptA(V34pBPA)-His_6 and *E. cloacae* pET22b-pelBss-LptA(I36pBPA)-His_6. Both were purified as described previously for *E. coli* LptA(I36pBPA)-His_6[4,10].

To test the activity of purified *V. cholerae* and *E. cloacae* $LptB_2FGC$ complexes, we reconstituted LPS release from liposomes to soluble LptA as described in detail in (ref. 16) with only minor modifications (Extended Data Fig. 1b). Briefly, purified $LptB_2FGC$ complexes, containing wild-type LptB or inactive LptB(E163Q), were incorporated into liposomes composed of *E. coli* polar lipids (Avanti Polar Lipids, Inc.) and Ra-LPS (Sigma) by the detergent dilution method. Proteoliposome stock solutions in 20 mM Tris-HCl (pH=8.0), 150 mM NaCl, and 10% v/v glycerol were mixed on ice with LptA(XpBPA)-His, 1 M Tris-HCL pH 8.0, 5 M NaCl, glycerol, and either ATP/$MgCl_2$ or ATP/EDTA such that the final concentrations of each were 60 %v/v proteoliposomes, 2 μM LptA, 500 mM NaCl, 50 mM Tris-HCl (pH=8.0), 5 mM ATP, and 2 mM $MgCl_2$ or 2 mM EDTA. Total volume was calculated such that 30 μL could be used per sample per timepoint. Stocks of ATP/Mg and ATP/EDTA were pre-mixed and added last, and after their addition the mixtures were moved from ice to 30 °C to initiate LPS transport. At the specified time points, 30 μL aliquots were transferred from the reaction mixtures to a 96-well plate on ice in which the aliquots were placed under a UV lamp (λ = 365 nm) for 1 min. Following UV-irradiation, samples were mixed 1:1 with 2x SDS gel loading buffer and analyzed by SDS-PAGE and western blotting with anti-LPS and anti-His_5 antibodies as described above.

Purification and reconstitution of *E. coli* $LptB_2FGC$ complexes

E. coli $LptB_2FGC$-His complexes containing wild-type LptF, LptF(S157C), LptF(I234C), or LptF(S157C/I234C) were prepared by a method similar to that described above for the *E. cloacae* homologs. C43 *E. coli* harboring pCDFduet-LptB-LptFG (or the appropriate LptF mutant) and pBADHisA-LptC-tbn-His_7 were diluted from overnight cultures into fresh LB + supplemented with 50 μg/mL carbenicillin and 50 μg/mL spectinomycin, grown at 37 °C. All cultures of cells harboring pCDFduet-LptB-LptF(S157C/I234C) were supplemented with 0.4% w/v glucose. At OD_{600} ~ 0.8, wild-type LptF, LptF(S157C), and LptF(I234C) cultures were cooled to 20 °C, induced by addition of 200 μM IPTG and 0.02% w/v L-

arabinose, and protein expression carried out for 16 h. Cultures expressing the LptF(S157C/I234C) variant were cooled to 30°C, induced, and protein expressed for 12 h. Thereafter, purification of wild-type and cysteine mutant $LptB_2FGC$-His complexes was identical to that for wild-type *E. cloacae* $LptB_2FGC$-His except that 0.5 mM THP was omitted from all buffers. *E. coli* LptA(I36pBPA)-His was purified as described previously[4,10].

E. coli $LptB_2FGC$-His complexes containing *p*BPA-substituted LptC – LptC(M19*p*BPA, G21*p*BPA, or F78*p*BPA) – were expressed in C43 cells containing pCDFduet-LptB-LptFG, pBADHisA-LptC-tbn-His_7 and pSup-BpaRS-6TRN as described above for wild-type complexes, except that 0.7mM *p*BPA was added to the media 15 minutes prior to induction. Purification of *p*BPA-substituted *E. coli* $LptB_2FGC$-His complexes was performed in the same manner as for the wild-type proteins.

Purified $LptB_2FGC$ complexes were incorporated into liposomes containing LPS by the detergent dilution method as described in detail in reference 4. LPS release from those liposomes to soluble LptA(I36pBPA) was carried out as described above, except that, in reactions in which it was present, 5 mM DTT was added to the liposome mixture 15 min prior to the addition of ATP/Mg.

Complementation and OM permeability assays with LptF cysteine mutants.

Growth Conditions.—Strains were grown in Lysogeny Broth (LB Lennox; Fisher Bioreagents) at 37 °C with aeration for liquid cultures and supplemented with 1.5% agar (DifcoTM; Becton Dickinson) for solid media. When necessary, media was supplemented with 125 μg/mL ampicillin (Sigma-Aldrich), 0.16 mM IPTG (Gold Biotechnology), and 33 μg/mL X-Gal (Gold Biotechnology). Strains are listed in Supplementary table 2.

Mutant Construction.—Plasmids encoding LptF variants were generated by site-directed mutagenesis PCR using the pBAD18LptFG3 plasmid[36] as template, Phusion polymerase (Fischer Scientific), and the primers listed in Supplementary Table 1 (Sigma-Aldrich). Complementation testing and generation of haploid strains was carried out as described previously[27,36].

OM Permeability Assays.—Assessment of OM permeability was carried out by disc-diffusion assay with bacitracin, novobiocin, rifampin and erythromycin discs (Becton Dickinson), as described previously[11].

Immunoblotting.—Levels for FLAG-tagged LptF variants were determined by immunoblotting whole-cell lysates normalized by OD_{600} with 1:10,000 dilution of anti-FLAG monoclonal antibody (Sigma-Aldrich) and horse-radish peroxidase conjugated with a 1:10,000 dilution of anti-mouse antibody (GE Healthcare Life Sciences), as described previously[27].

Measurement of ATP hydrolysis by $LptB_2FGC$ in liposomes – LptF cysteine mutants

ATPase assays were done using a the EnzChek® Phosphate Assay Kit (Molecular Probes) at 30 °C as previously reported[37]. A 90 μL reaction mixture containing 20 μL of the supplied substrate, 1 μL of the supplied enzyme, 28 mM Tris (pH=8.0), 304 mM NaCl, 6.7%

glycerol, 5.6 mM ATP and 2.2 mM $MgCl_2$ was incubated at room temperature for 5 minutes to allow the consumption of contaminating phosphate. Reactions were initiated by the addition of 10 μL proteoliposomes solution, and the absorbance at wavelength of 360 nm was monitored using an Epoch microplate spectrophotometer. Rates are the slope of the linear region of the product formation graph. Error bars indicate the standard deviations of the rates measured over 3 biological and technical replicates.

Measurement of ATP hydrolysis in liposomes – comparison of $LptB_2FG$, $LptB_2FGC$, and $LptB_2FGC$ + ΔTM-LptC

ATPase activity was assayed using a modified molybdate method, as previously reported[38]. All assays were done in 50 mM Tris-HCl (pH 8.0), 500 mM NaCl, 10% glycerol (final concentrations). Reactions contained 60% proteoliposomes by volume (prepared as described above, thawed on ice). The remaining volume was composed of Tris-HCl, NaCl, and glycerol such that the final concentrations would be the values listed above. Soluble LptC was added at the indicated molar rations and incubated with the proteoliposomes for 15 minutes on ice. Reactions were initiated at 30°C with the addition of ATP/$MgCl_2$ (5 mM ATP, 2 mM $MgCl_2$). Aliquots were taken at 0, 20, 40, and 60 minutes and were quenched with an equal volume of 12% sodium dodecyl sulfate (SDS, Sigma). Inorganic phosphate was measured using the reported method[38]. Absorbance values were measured using a Spectramax Plus 384 plate reader (Molecular Devices). The experiment was repeated three times for each condition. For analysis, linear lines of best fit were calculated for each replicate data set. Plotted data represents the mean value of the slopes and the error bars indicate the standard deviation.

Supplementary Material

Refer to Web version on PubMed Central for supplementary material.

Extended Data

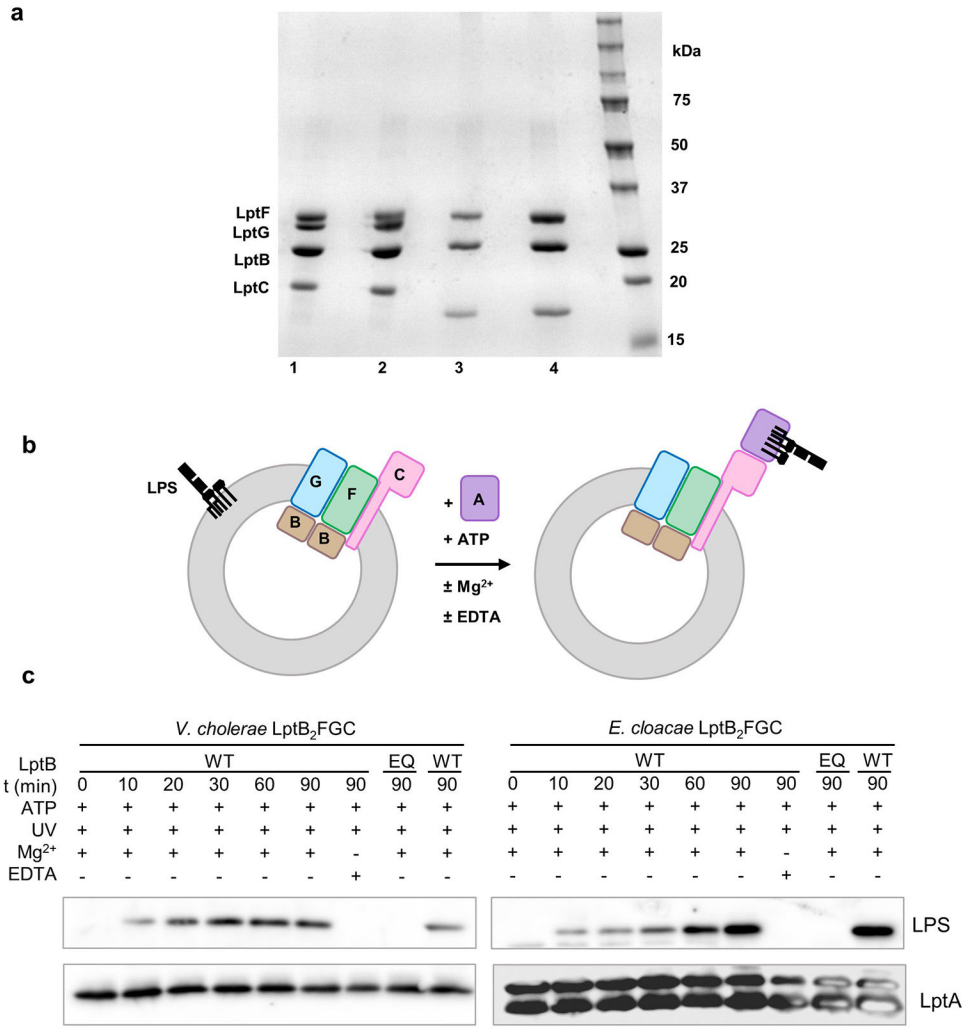

Extended Data Figure 1: Purification and reconstitution of wild-type and inactive complexes of *V. cholerae* and *E. cloacae* $LptB_2FGC$.

(**a**) To assess the protein quality in purified $LptB_2FGC$ complexes, samples were boiled in SDS-loading buffer, separated by polyacrylamide gel electrophoresis (PAGE) using a 4–20% gradient polyacrylamide gel, and then stained with Coomassie Brilliant Blue dye. (1) wild-type, *E. cloacae*, (2) catalytically inactive LptB(E163Q), *E. cloacae*, (3) wild-type, *V. cholerae*, and (4) catalytically inactive LptB(E163Q), *V. cholerae*. Note that *V. cholerae* LptF and LptG co-migrate in this gel, but can be separated under other conditions. Protein samples are each representative of 10 or more replicates. (**b**) Schematic of a reconstitution of lipopolysaccharide transport in which purified $LptB_2FGC$ and LPS have been incorporated into liposomes by the detergent-dilution method. Addition of LptA modified with a photocrosslinkable amino acid (I36pBPA for *E. cloacae*, V34pBPA for *V. cholerae*), along with ATP and Mg^{2+} leads to time dependent accumulation of LPS in LptA. LPS transport is monitored by exposing the samples to UV light at the time point shown, quenching transport by addition of SDS-loading buffer, PAGE to separate LPS-LptA adducts from LPS, and finally western blotting against LPS. (**c**) Results of the experiment described in (B) - anti-LPS blots show time dependent accumulation of LPS in LptA when the proteoliposomes

contain wild-type $LptB_2FGC$ complexes, but accumulation of LPS is not observed when EDTA is substituted for Mg^{2+}, or when the complexes contain LptB(E163Q) rather than wild-type LptB. Anti-His_5 blots were used to assess the amount of LptA (XpBPA)-His in each sample. *E. coli* and *E. cloacae* LptA(I36pBPA)-His_6 run as a doublet whereas *V. cholerae* LptA(I36pBPA)-His_6 does not. Blots are representative of data from three biological replicates.

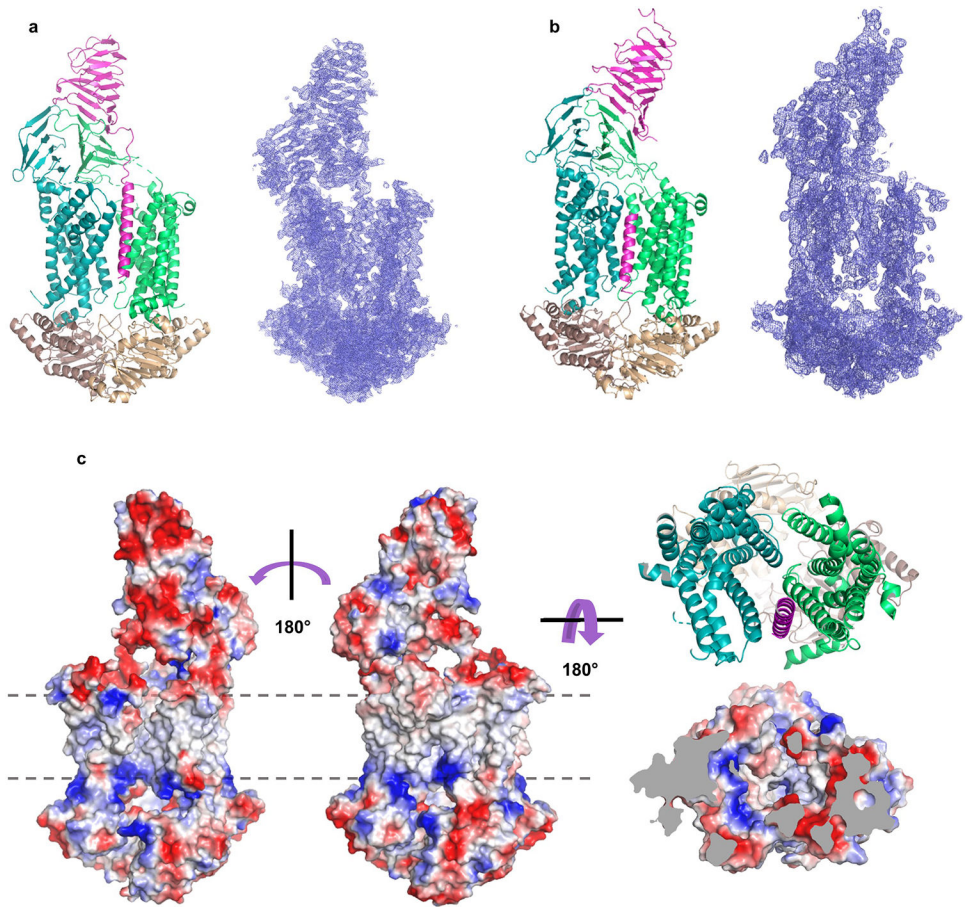

Extended Data Figure 2: Structures *V. cholerae* LptB(E163Q)$_2$FGC and *E. cloacae* LptB$_2$FGC with their electron density maps.

(**a**) Ribbon diagram of *V. cholera* LptB(E163Q)$_2$FGC (left) and corresponding 2Fo-Fc simulated-annealing composite omit map (right) contoured at 1.0 σ. and carved 2.5 Å from the model. (**b**) Ribbon diagram of *E. cloacae* LptB$_2$FGC (left) and corresponding 2Fo-Fc simulated-annealing composite omit map (right) contoured at 1.0 σ. and carved at 2.5 Å from the model. **(c**) Electrostatic surface potential of *V. cholerae* LptB(E163Q)$_2$FGC depicted with the most basic residues in blue and most acidic residues in red. The approximate edges of the inner membrane are denoted with grey dashed lines. The central panel is in the same orientation as in (a). The left panel is a 180° rotation around the axis perpendicular to the membrane. In the right panel, the view in the central panel has been rotated 180° around an axis parallel to the membrane in the plane of the page, and the periplasmic domains clipped away to give a view of the central cavity between the transmembrane helices. For reference, a ribbon diagram (analogous to Fig 1c) is displayed above.

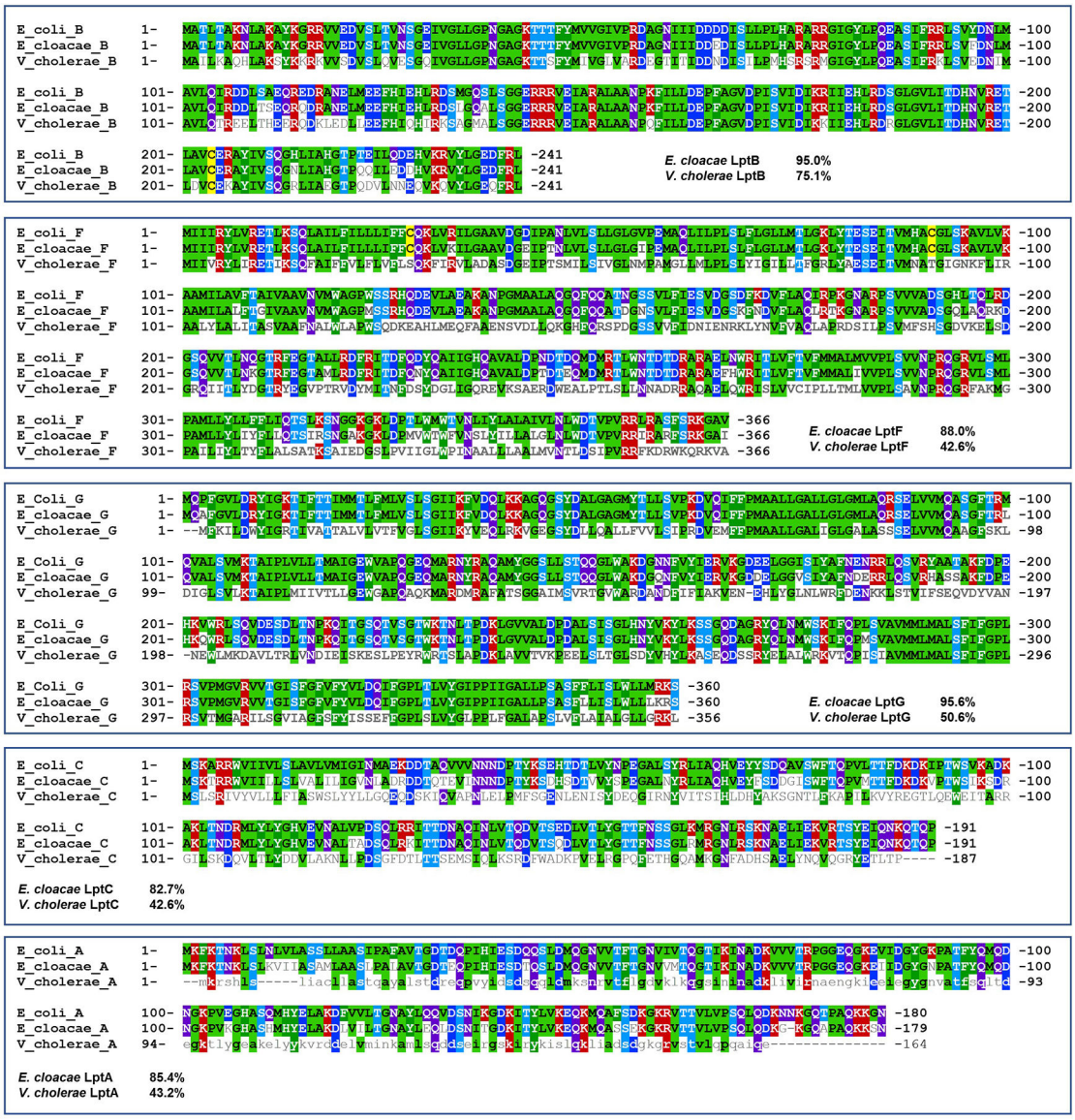

Extended Data Figure 3: Alignments of *E. coli*, *E. cloacae*, and *V. cholerae* LptB, LptF, LptG, LptC, and LptA.

(**a**) Sequences of Lpt proteins from *Escherichia coli* K12, *Enterobacter cloacae subsp. cloacae* ATCC 13047 and *Vibrio cholerae* C6706. Percent identity of the *E. cloacae* and *V. cholerae* sequences to the *E. coli* sequence are listed after each alignment. Note that public databases (including Uniprot, NCBI) contain a misannotated LptF sequence for *Enterobacter cloacae subsp. cloacae* ATCC 13047, with bases GTGATAATCATAAGATATCTG missing from the beginning of LptF; LptF homologs from other *Enterobacter cloacae* strains do not appear to contain this error. Alignments were made using ClustalO and then colored in MView (https://www.ebi.ac.uk/Tools/msa/clustalo/).

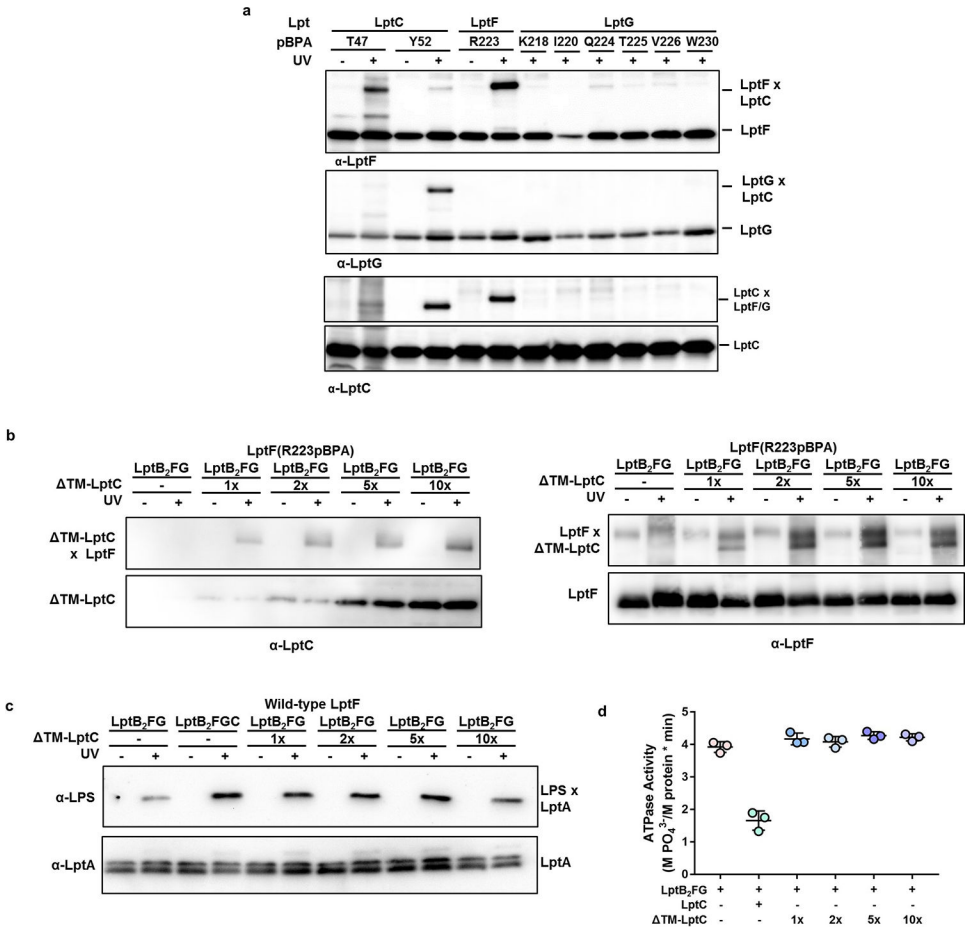

Extended Data Figure 4: ΔTM-LptC stably associates with LptB$_2$FG, and facilitates LPS release to LptA as well as full-length LptC without altering the ATPase activity of LptB$_2$FG.

(**a**) *In vivo* photocrosslinking experiment from Fig. 2b, shown with the corresponding anti-LptC western blot. (**b**) *In vivo* photocrosslinking experiments (Fig. 2) showed that a *p*BPA substitution at position R223 of LptF could form LptF-LptC adducts after exposure to UV light. In this experiment, proteoliposomes containing LptF, LptB$_2$F(R223*p*BPA)G were incubated with soluble ΔTM-LptC at 1x, 2x, 5x, or 10x molar excess of LptC and then exposed to UV light to test whether ΔTM-LptC associated with the LptB$_2$F(R223*p*BPA)G complexes. Anti-LptC (left) and anti-LptF (right) western blots were used to assess the amount of LptC-LptF adduct formed (top panels) as well as the amounts of LptC and LptF in each sample (bottom panel). The anti-LptF and anti-LptC blots were performed on the same set of samples. The intensity of the LptC-LptF adduct band does not increase with ΔTM-LptC beyond 2x to 5x molar excess. This result suggests that at those concentrations of ΔTM-LptC, the binding site for ΔTM-LptC at LptF(R223*p*BPA) is saturated. The intensity of the LptF band (bottom right panel) does not decrease further because residues R223*p*BPA can also form intramolecular crosslinks to other parts of the LptF β-jellyroll, and these may be favored over intermolecular crosslinks to ΔTM-LptC. (**c**), (**d**) Figs. 2c, d shown with 5x and 10x molar excess of ΔTM-LptC. Blots shown in (a), (b) and (c) are representative of data from 3 biological replicates.

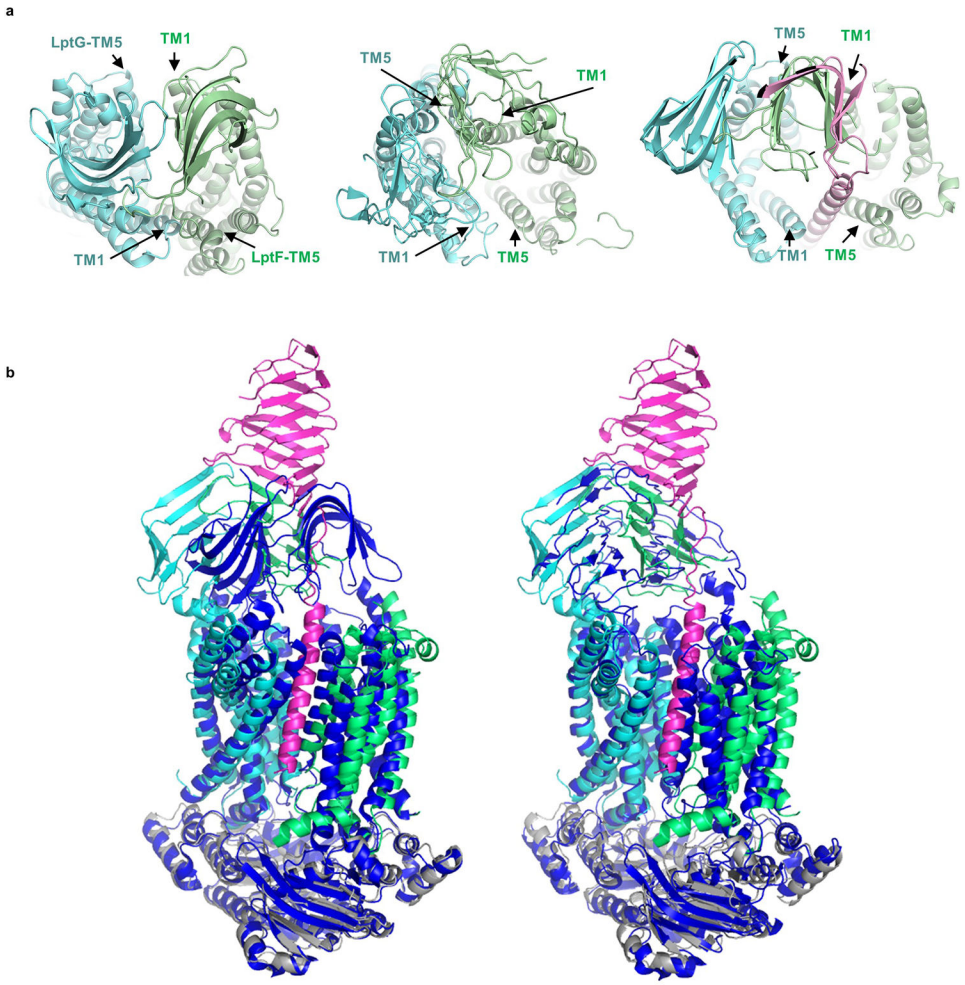

Extended Data Figure 5: Comparison of previously published $LptB_2FG$ structures to the structure of *V. cholerae* $LptB_2FGC$.

(**a**) Top-down views of the *P. aeruginosa* $LptB_2FG$ structure (left panel, PDB #5×5y)[20], *K. pneumoniae* $LptB_2FG$ structure (center panel, PDB #5l75)[19] and our *V. cholera* $LptB_2FGC$ structure (right panel). (**b**) Alignments of *P. aeruginosa* $LptB_2FG$ (left, colored dark blue) and *K. pneumoniae* $LptB_2FG$ (right, colored dark blue) with *V. cholerae* $LptB_2FGC$ (LptC is colored pink, LptF is colored green, LptG is colored teal, and LptB is colored grey.)

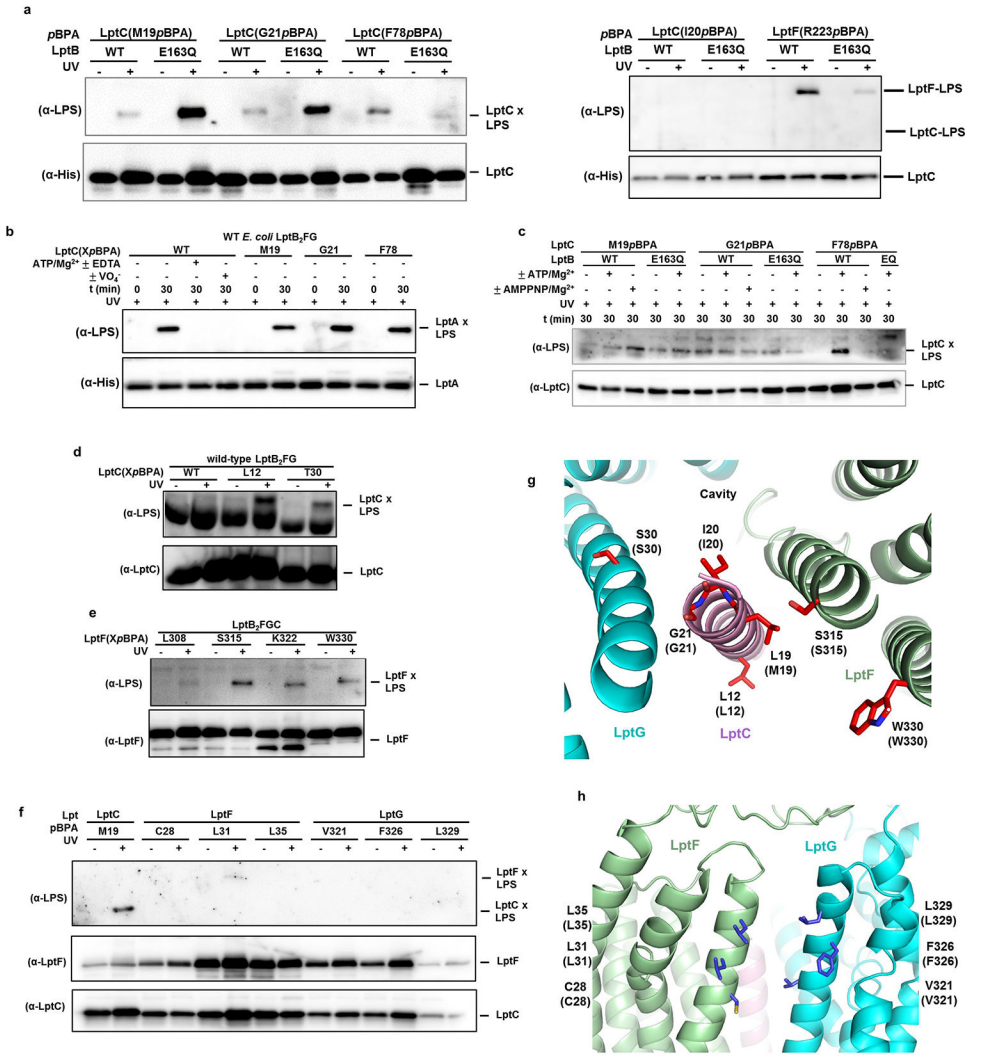

Extended Data Figure 6: LPS enters the cavity of $LptB_2FGC$ via LptG-TM1, LptF-TM5 and the LptC-TM helix in a nucleotide-independent manner.

(**a**) Figure 3b is show alongside additional *in vivo* photocrosslinking experiments comparing LPS crosslinking in wild-type and LptB(E163Q) backgrounds. (**b**) *In vitro* reconstitution (as in Extended Data Fig. 1b) of $LptB_2FGC$, $LptB_2FGC$(M19*p*BPA), $LptB_2FGC$(G21*p*BPA), and $LptB_2FGC$(F78*p*BPA) shows that the variants with amber codons incorporated in the LptC TM helix release LPS to LptA(I36*p*BPA) as well as wild-type. (**c**) *In vitro* photocrosslinking of $LptB_2FGC$ *p*BPA variants reconstituted into proteoliposomes with LPS, as in figure 3d, comparing complexes containing LptB(E163Q) to those containing wild-type-LptB, and the effects of AMPPNP relative to ATP. (**d-f**) Additional crosslinking experiments with *p*BPA incorporated at other positions in the TM helix of LptC, LptF TM1 and TM5, and LptG TM1 and TM5. (**g**), (**h**) Ribbon diagrams of *E. cloacae* $LptB_2FGC$, with views of the two potential gates in the LptFGC transmembrane helices; LptG (teal), LptC (pink), and LptF (green). Residues of interest are shown as sticks. Blots for LptG(S30pBPA) are show in Extended data Fig 7b. Blots shown in (a-f) are representative of data from 3 biological replicates.

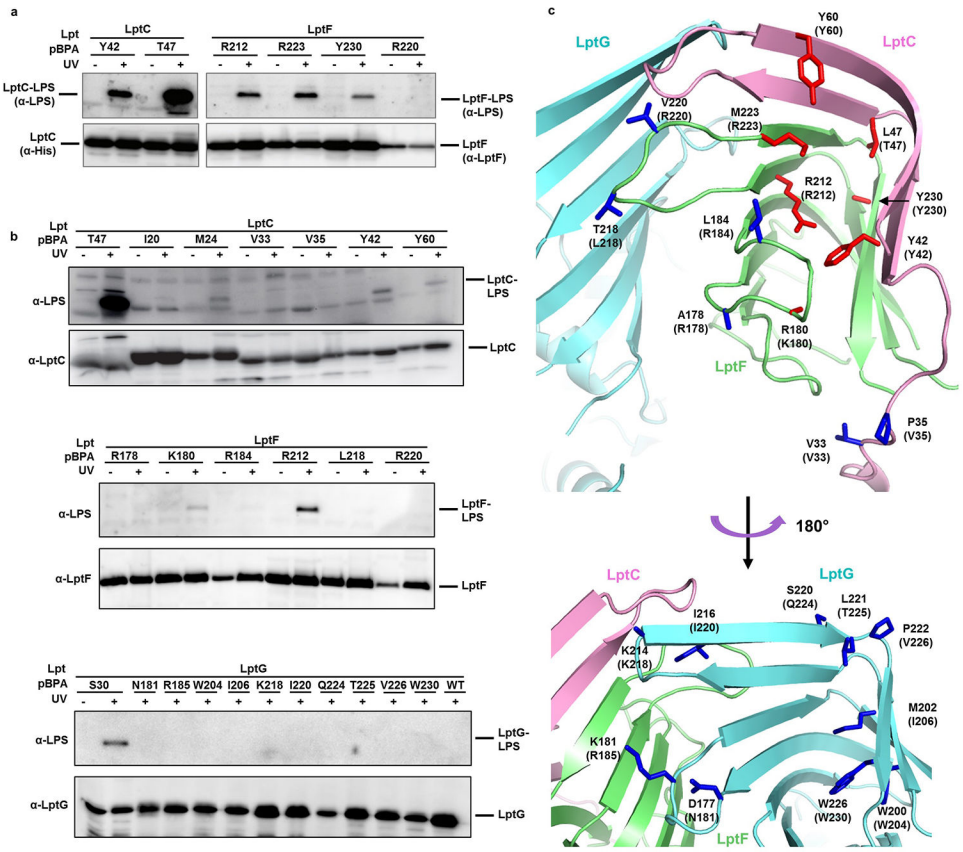

Extended Data Figure 7: *In vivo* photocrosslinking experiments show that LPS passes through the β-jellyroll domains of LptF and LptC, but not LptG.

(**a**) Fig. 3C shown for reference. (**b**). *In vivo* photocrosslinking experiments performed analogously to those in Fig. 3b,c. The UV-photocrosslinkable amino acid pBPA was substituted at positions in the periplasmic β-jellyroll domains of LptC, LptF, and LptG. Positions in the interior of the LptF and LptC can crosslink to LPS, whereas those facing outside the β-jellyroll do not. No crosslinks to LPS were observed at 10 positions in the LptG β-jellyroll; in contrast, LptG(S30pBPA), in TM helix 1 and facing the cavity of the transmembrane domain, can crosslink LPS. (**c**) Ribbon diagram of the *V. cholerae* structure showing the β-jellyroll domains of LptC, LptF, and LptG. Sidechains of residues that crosslink LPS are colored red, whereas residues which do not crosslink LPS are colored blue. Blots shown in (a) and (b) are representative of data from 3 biological replicates.

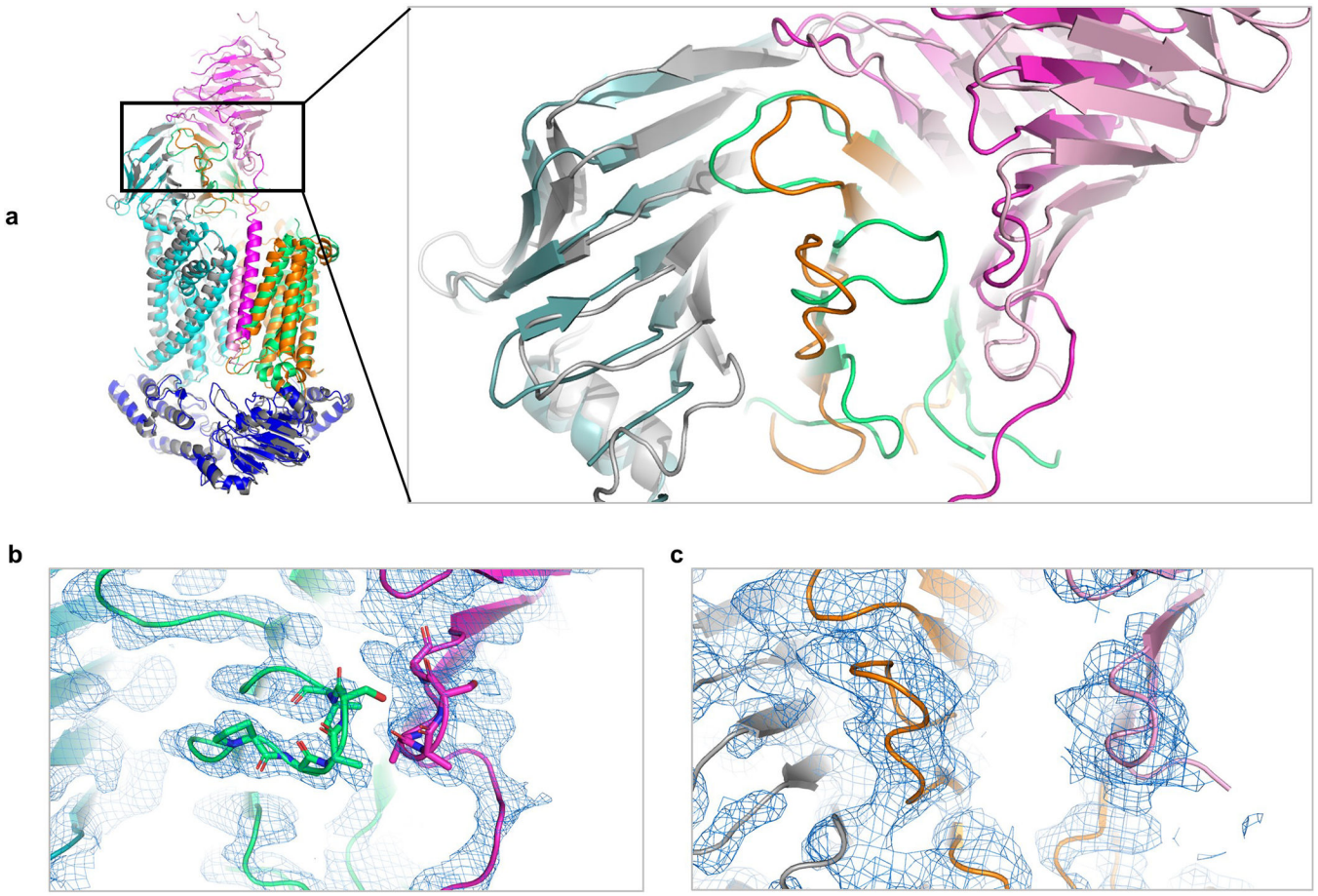

Extended Data Figure 8: Comparison of the *V. cholerae* and *E. cloacae* structures reveals two states of the gate in LptF.

(**a**) An overlay of the *V. cholerae* (LptG, teal; LptF, green; LptC, magenta) and *E. cloacae* (LptG, gray; LptF, orange; LptC, pink) structures shows two conformations of the loop between the third and fourth β –strands of the LptF periplasmic domain. (**b**) Closeup view of that loop and an adjacent loop from LptC in the *V. cholerae* structure. Residues LptF 179–183 and LptC 71–74 are depicted as sticks on top of the cartoon (**c**) Closeup view of the same region in *E. cloacae*. The 2Fo-Fc omit maps in (b) and (c) are contoured at 1.0 σ and carved 2.5 Å from the protein.

a

Relevant genotype	Complements Δ*lptF*
WT	Yes
LptFG$^+$	Yes
LptF-FLAG	Yes
LptF(S157C)-FLAG	Yes
LptF(I234C)-FLAG	Yes
LptF(S157C/I234C)-FLAG	No

b

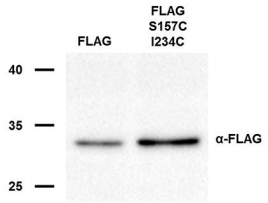

c

OM permeability of halploid LptF cysteine mutants

Strain	Relevant genotype	Zone of inhibition (mm) Bacitracin	Novobiocin	Erythromycin	Rifampin
NR2761	*lptF*$^+$	(10.0)±(1.0)	(10.2)±(0.3)	(15.2)±(1.0)	10.3(14.2)±0.3(0.3)
NR5593	*lptF(180FLAG)*	(10.7)±(0.6)	(10.5)±(0.5)	(15.5)±(0.5)	11.0(14.5)±0.8(0.5)
NR5686	*lptF(180FLAG/S157C)*	(10.8)±(0.3)	(10.7)±(0.6)	(15.5)±(0.5)	10.2(14.7)±0.9(0.6)
NR5687	*lptF(180FLAG/I234C)*	(10.7)±(0.3)	(10.7)±(0.6)	(15.5)±(0.5)	11.2(14.5)±0.9(0.9)

d

OM permeability of merodiploid LptF cysteine mutants

Strain	Relevant genotype[b]	Zone of inhibition (mm) Bacitracin	Novobiocin	Erythromycin	Rifampin
NR5710	*lptF(180FLAG)lptG*$^+$ / *lptFG*$^+$	(10)±(0.4)	(9.9)±(0.6)	(13.4)±(0.3)	8.6(12)±0.5(0)
NR5712	*lptF(180FLAG/S157C)lptG*$^+$ / *lptFG*$^+$	(9.8) ±(0.3)	(10)±(0.6)	(13.1)±(0.3)	8.6(11.9)±0.3(0.3)
NR5713	*lptF(180FLAG/I234C)lptG*$^+$ / *lptFG*$^+$	(10.1)±(0.3)	(9.4)±(0.3)	(14.8)±(0.6)	8.5(11.3)±0.4(0.5)
NR5714	*lptF(180FLAG/S157C/I234C)lptG*$^+$ / *lptFG*$^+$	(9.9)±(0.3)	9.1(13.5)±0.5(0.7)	10.5(15)±1.1(0.7)	9.9(17.6)±0.3(1.9)

e

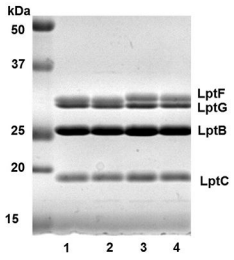

f

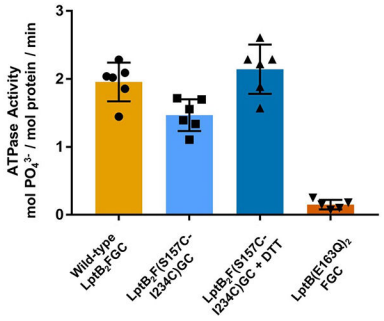

Extended Data Figure 9: Complementation and purification of LptF cysteine mutants.

(**a**) Table of results from assays which tested the ability of plasmids encoding *E. coli* LptF variants to complement a *ΔLptF* strain. (**b**) To assess whether the LptF double-cysteine mutant was being expressed and translated properly, we measured LptF-FLAG levels by anti-FLAG western blot in whole-cell lysates from merodiploid *E. coli* strains containing either pBAD18-LptF-FLAG or pBAD18-LptF(S157C/I234C)-FLAG. (**c**) Disc diffusion assays were carried out to assess the OM permeability (relative to wild-type) of *E. coli* strains expressing only plasmid-encoded LptF variants. Values denote the diameter of regions of no growth in mm, and values in parentheses denote regions of inhibited growth. Discs were 6 mm in diameter. (**d**) Disc diffusion assays were performed as in (c), accept that experiments were performed in merodiploid strains with wild-type chromosomal copies of *lptFG*. Alleles are listed as follows: plasmid encoded *lptFG* alleles, followed by a slash, followed by chromosomally encoded *lptFG* alleles. (**e**) Coomassie-stained samples of purified $LptB_2FGC$ used in the LPS release assay, (1) LptF-FLAG, (2) LptF(S157C)-FLAG, (3) LptF(I234C)-FLAG, or (4) LptF(S157C/I234C)-FLAG. LptC had a C-terminal thrombin-His_7 tag used for nickel-affinity chromatography which was cleaved prior to reconstitution into liposomes. (**f**) The ATPase activity of *E. coli* $LptB_2FGC$ reconstituted into liposomes was assessed by measuring the rate of phosphate release over time. Error bars

show the standard deviation of results from three technical replicates each of two biological replicates, except two replicates were performed with one LptB(E163Q)$_2$FGC sample. Data shown in (b) and (e) are representative of data from 3 biological replicates. The results shown in (c) and (d) are averages ± standard deviations calculated from three independent experiments.

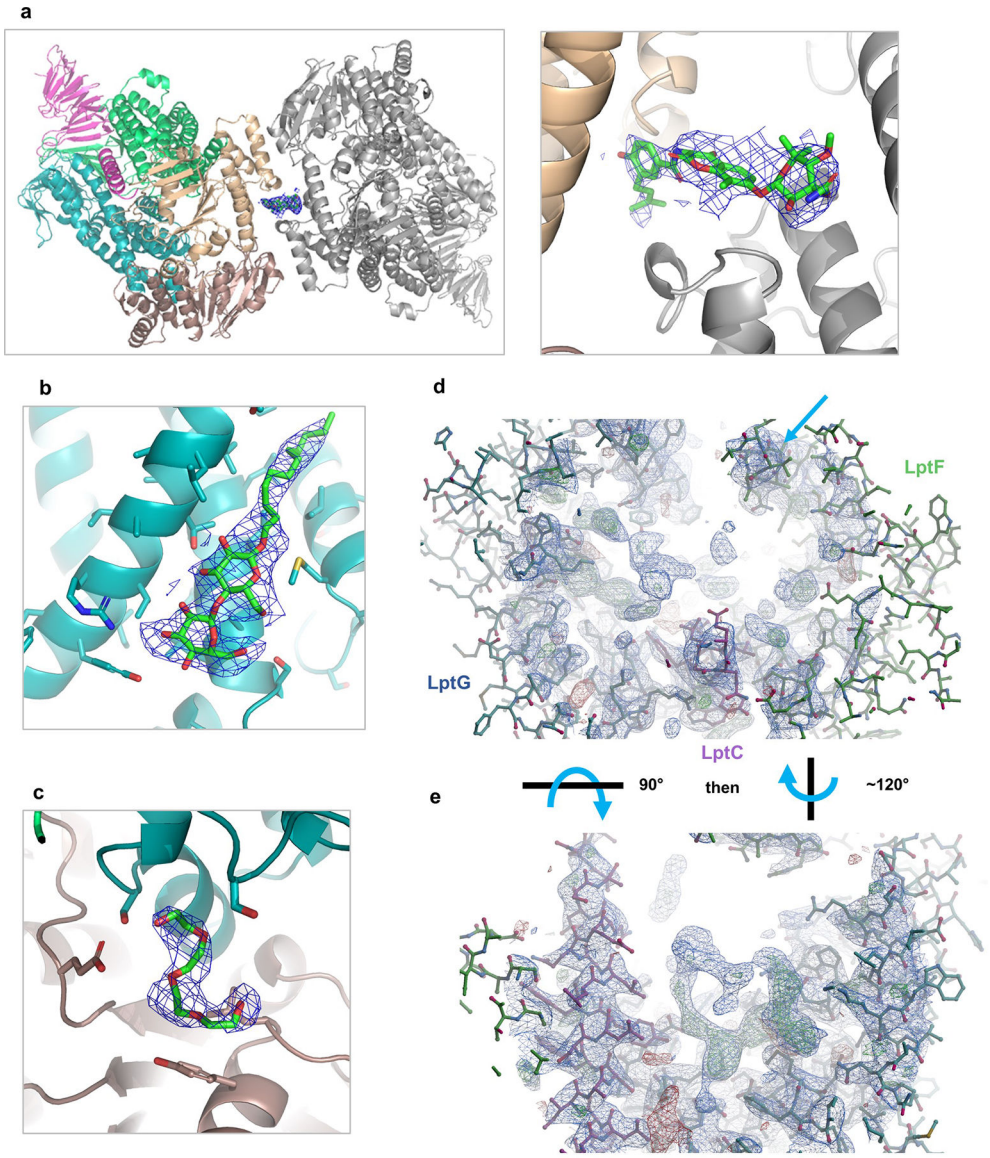

Extended Data Figure 10: Examples of small molecules bound in the crystal structures of *V. cholerae* and *E. cloacae* LptB$_2$FGC, and unmodeled electron density in the *V. cholerae* LptB(E163Q)$_2$FGC structure.

(**a**) Two views of the one molecule of novobiocin bound at the interface between two non-crystallographically symmetric copies of *E. cloacae* LptB, with 2Fo-Fc simulated-annealing composite omit map contoured at 1.5 σ and carved at 2.0 Å. (**b**) Electron density for several ordered detergent molecules is present in the structure of *V. cholerae* LptB$_2$FGC; here, a DDM is shown bound to LptG with an Fo-Fc Polder map contoured at 2.5 σ. (**c**) Ordered PEG400 at the interface of *V. cholerae* LptB and LptG, with the 2Fo-Fc map contoured at 1.0 σ and carved at 2.0 Å. (**d**) View of the lumen between the transmembrane helices of LptC (purple, at bottom), LptF (green, at right), and LptG (teal, at left), looking towards the inner membrane from the periplasm. 2Fo-Fc map contoured at 1.0 σ (blue mesh) and Fo-Fc map contoured at 3.0 σ (green and red meshes). (**e**) View of the same region from within the

membrane, with LptF helices in the foreground clipped away; the perspective is approximated by the teal arrow at the top right of panel (d).

Acknowledgements:

The authors would like to thank Jue Chen and Mike Oldham (Rockefeller University) for helpful conversations in the early stages of the project. This work used GM/CA and NE-CAT beamlines (P30 GM124165) at the APS synchrotron source (DE-AC02–06CH11357), and an Eiger detector (S10OD021527). We thank the NE-CAT and GM/CA beamline staff for support during X-ray data collection. This work was supported by grants R01GM100951 to N.R., U19 AI109764 to ACK, and R01 GM066174 and R01 AI081059 to D.K.

References

1. Whitfield C & Trent MS Biosynthesis and export of bacterial lipopolysaccharides. Annu Rev Biochem 83, 99–128, doi:10.1146/annurev-biochem-060713-035600 (2014). [PubMed: 24580642]
2. Okuda S, Sherman DJ, Silhavy TJ, Ruiz N & Kahne D Lipopolysaccharide transport and assembly at the outer membrane: the PEZ model. Nat Rev Microbiol 14, 337–345, doi:10.1038/nrmicro.2016.25 (2016). [PubMed: 27026255]
3. Chng SS, Gronenberg LS & Kahne D Proteins required for lipopolysaccharide assembly in Escherichia coli form a transenvelope complex. Biochemistry 49, 4565–4567, doi:10.1021/bi100493e (2010). [PubMed: 20446753]
4. Sherman DJ et al. Lipopolysaccharide is transported to the cell surface by a membrane-to-membrane protein bridge. Science 359, 798–801, doi:10.1126/science.aar1886 (2018). [PubMed: 29449493]
5. Narita S & Tokuda H Biochemical characterization of an ABC transporter LptBFGC complex required for the outer membrane sorting of lipopolysaccharides. FEBS Lett 583, 2160–2164, doi:10.1016/j.febslet.2009.05.051 (2009). [PubMed: 19500581]
6. Ruiz N, Gronenberg LS, Kahne D & Silhavy TJ Identification of two inner-membrane proteins required for the transport of lipopolysaccharide to the outer membrane of Escherichia coli. Proc Natl Acad Sci U S A 105, 5537–5542, doi:10.1073/pnas.0801196105 (2008). [PubMed: 18375759]
7. Sperandeo P et al. Characterization of lptA and lptB, two essential genes implicated in lipopolysaccharide transport to the outer membrane of Escherichia coli. J Bacteriol 189, 244–253, doi:10.1128/JB.01126-06 (2007). [PubMed: 17056748]
8. Davidson AL, Dassa E, Orelle C & Chen J Structure, function, and evolution of bacterial ATP-binding cassette systems. Microbiol Mol Biol Rev 72, 317–364, table of contents, doi:10.1128/MMBR.00031-07 (2008). [PubMed: 18535149]
9. Thomas C & Tampe R Multifaceted structures and mechanisms of ABC transport systems in health and disease. Curr Opin Struct Biol 51, 116–128, doi:10.1016/j.sbi.2018.03.016 (2018). [PubMed: 29635113]
10. Okuda S, Freinkman E & Kahne D Cytoplasmic ATP hydrolysis powers transport of lipopolysaccharide across the periplasm in E. coli. Science 338, 1214–1217, doi:10.1126/science.1228984 (2012). [PubMed: 23138981]
11. Sherman DJ et al. Decoupling catalytic activity from biological function of the ATPase that powers lipopolysaccharide transport. Proc Natl Acad Sci U S A 111, 4982–4987, doi:10.1073/pnas.1323516111 (2014). [PubMed: 24639492]
12. Sperandeo P et al. Functional analysis of the protein machinery required for transport of lipopolysaccharide to the outer membrane of Escherichia coli. J Bacteriol 190, 4460–4469, doi:10.1128/JB.00270-08 (2008). [PubMed: 18424520]
13. Wu T et al. Identification of a protein complex that assembles lipopolysaccharide in the outer membrane of Escherichia coli. Proc Natl Acad Sci U S A 103, 11754–11759, doi:10.1073/pnas.0604744103 (2006). [PubMed: 16861298]
14. Freinkman E, Chng SS & Kahne D The complex that inserts lipopolysaccharide into the bacterial outer membrane forms a two-protein plug-and-barrel. Proc Natl Acad Sci U S A 108, 2486–2491, doi:10.1073/pnas.1015617108 (2011). [PubMed: 21257904]

15. Chng SS, Ruiz N, Chimalakonda G, Silhavy TJ & Kahne D Characterization of the two-protein complex in Escherichia coli responsible for lipopolysaccharide assembly at the outer membrane. Proc Natl Acad Sci U S A 107, 5363–5368, doi:10.1073/pnas.0912872107 (2010). [PubMed: 20203010]
16. Bos MP, Tefsen B, Geurtsen J & Tommassen J Identification of an outer membrane protein required for the transport of lipopolysaccharide to the bacterial cell surface. Proc Natl Acad Sci U S A 101, 9417–9422, doi:10.1073/pnas.0402340101 (2004). [PubMed: 15192148]
17. Braun M & Silhavy TJ Imp/OstA is required for cell envelope biogenesis in Escherichia coli. Molecular Microbiology 45, 1289–1302, doi:DOI 10.1046/j.1365-2958.2002.03091.x (2002). [PubMed: 12207697]
18. Tran AX, Dong C & Whitfield C Structure and functional analysis of LptC, a conserved membrane protein involved in the lipopolysaccharide export pathway in Escherichia coli. J Biol Chem 285, 33529–33539, doi:10.1074/jbc.M110.144709 (2010). [PubMed: 20720015]
19. Dong H, Zhang Z, Tang X, Paterson NG & Dong C Structural and functional insights into the lipopolysaccharide ABC transporter LptB2FG. Nat Commun 8, 222, doi:10.1038/s41467-017-00273-5 (2017). [PubMed: 28790314]
20. Luo Q et al. Structural basis for lipopolysaccharide extraction by ABC transporter LptB2FG. Nat Struct Mol Biol 24, 469–474, doi:10.1038/nsmb.3399 (2017). [PubMed: 28394325]
21. Locher KP Mechanistic diversity in ATP-binding cassette (ABC) transporters. Nat Struct Mol Biol 23, 487–493, doi:10.1038/nsmb.3216 (2016). [PubMed: 27273632]
22. Ryu Y & Schultz PG Efficient incorporation of unnatural amino acids into proteins in Escherichia coli. Nat Methods 3, 263–265, doi:10.1038/nmeth864 (2006). [PubMed: 16554830]
23. Villa R et al. The Escherichia coli Lpt transenvelope protein complex for lipopolysaccharide export is assembled via conserved structurally homologous domains. J Bacteriol 195, 1100–1108, doi:10.1128/JB.02057-12 (2013). [PubMed: 23292770]
24. Putker F, Bos MP & Tommassen J Transport of lipopolysaccharide to the Gram-negative bacterial cell surface. FEMS Microbiol Rev 39, 985–1002, doi:10.1093/femsre/fuv026 (2015). [PubMed: 26038291]
25. Bertani BR, Taylor RJ, Nagy E, Kahne D & Ruiz N A cluster of residues in the lipopolysaccharide exporter that selects substrate variants for transport to the outer membrane. Mol Microbiol, doi:10.1111/mmi.14059 (2018).
26. Benedet M et al. The Lack of the Essential LptC Protein in the Trans-Envelope Lipopolysaccharide Transport Machine Is Circumvented by Suppressor Mutations in LptF, an Inner Membrane Component of the Escherichia coli Transporter. PLoS One 11, e0161354, doi:10.1371/journal.pone.0161354 (2016). [PubMed: 27529623]
27. May JM et al. The Antibiotic Novobiocin Binds and Activates the ATPase That Powers Lipopolysaccharide Transport. J Am Chem Soc 139, 17221–17224, doi:10.1021/jacs.7b07736 (2017). [PubMed: 29135241]
28. Kabsch W Xds. Acta Crystallogr D Biol Crystallogr 66, 125–132, doi:10.1107/S0907444909047337 (2010). [PubMed: 20124692]
29. Winn MD et al. Overview of the CCP4 suite and current developments. Acta Crystallogr D Biol Crystallogr 67, 235–242, doi:10.1107/S0907444910045749 (2011). [PubMed: 21460441]
30. Evans PR & Murshudov GN How good are my data and what is the resolution? Acta Crystallogr D Biol Crystallogr 69, 1204–1214, doi:10.1107/S0907444913000061 (2013). [PubMed: 23793146]
31. McCoy AJ et al. Phaser crystallographic software. J Appl Crystallogr 40, 658–674, doi:10.1107/S0021889807021206 (2007). [PubMed: 19461840]
32. Adams PD et al. PHENIX: a comprehensive Python-based system for macromolecular structure solution. Acta Crystallogr D Biol Crystallogr 66, 213–221, doi:10.1107/S0907444909052925 (2010). [PubMed: 20124702]
33. Emsley P & Cowtan K Coot: model-building tools for molecular graphics. Acta Crystallogr D Biol Crystallogr 60, 2126–2132, doi:10.1107/S0907444904019158 (2004). [PubMed: 15572765]
34. Afonine PV et al. Towards automated crystallographic structure refinement with phenix.refine. Acta Crystallogr D Biol Crystallogr 68, 352–367, doi:10.1107/S0907444912001308 (2012). [PubMed: 22505256]

35. Freinkman E, Okuda S, Ruiz N & Kahne D Regulated assembly of the transenvelope protein complex required for lipopolysaccharide export. Biochemistry 51, 4800–4806, doi:10.1021/bi300592c (2012). [PubMed: 22668317]

36. Simpson BW et al. Identification of Residues in the Lipopolysaccharide ABC Transporter That Coordinate ATPase Activity with Extractor Function. Mbio 7, doi:10.1128/mBio.01729-16 (2016).

37. Matano LM et al. Antibiotic That Inhibits the ATPase Activity of an ATP-Binding Cassette Transporter by Binding to a Remote Extracellular Site. J Am Chem Soc 139, 10597–10600, doi:10.1021/jacs.7b04726 (2017). [PubMed: 28727445]

38. Chifflet S, Torriglia A, Chiesa R & Tolosa S A method for the determination of inorganic phosphate in the presence of labile organic phosphate and high concentrations of protein: application to lens ATPases. Anal Biochem 168, 1–4 (1988). [PubMed: 2834977]

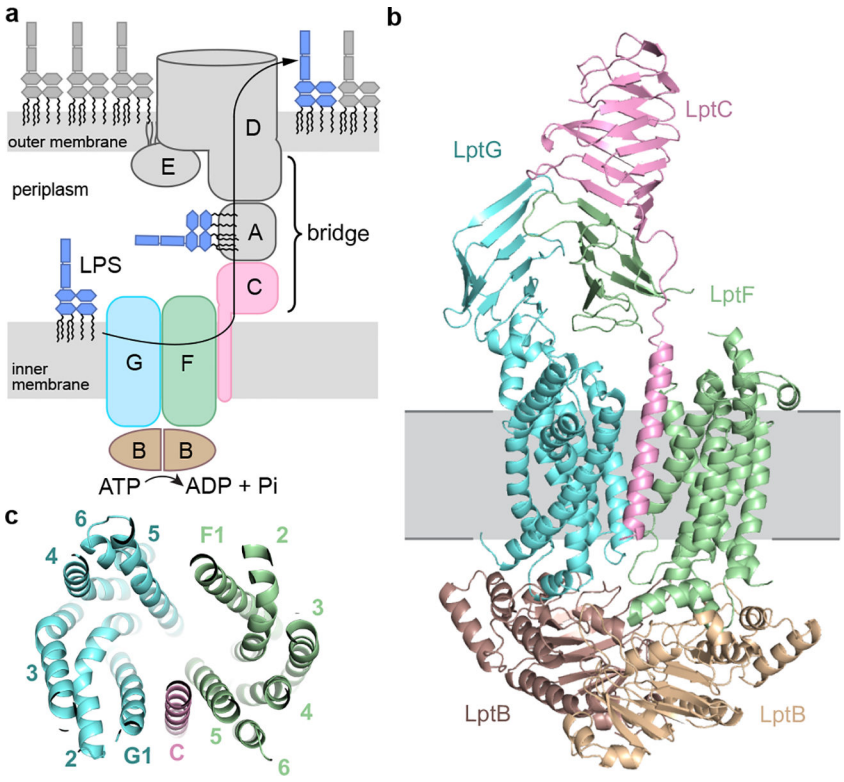

Figure 1: Crystal structure of the inner-membrane complex of the LPS transport machine.

(**a**) A schematic showing the seven protein components of the lipopolysaccharide transport (Lpt) machine and movement of LPS from the inner membrane to the outer leaflet of the outer membrane. The soluble protein LptA, and the periplasmic domains of LptC and LptD, form a protein 'bridge' across the aqueous periplasm. (**b**) Ribbon diagram of *V. cholerae* $LptB_2FGC$, with LptC colored pink, the two copies of the ATPase, LptB, colored brown and the transmembrane components, LptF and LptG, colored green and blue, respectively. The membrane is denoted in grey. (**c**) Ribbon diagram depicting the view from the periplasm into the cavity between the transmembrane helices.

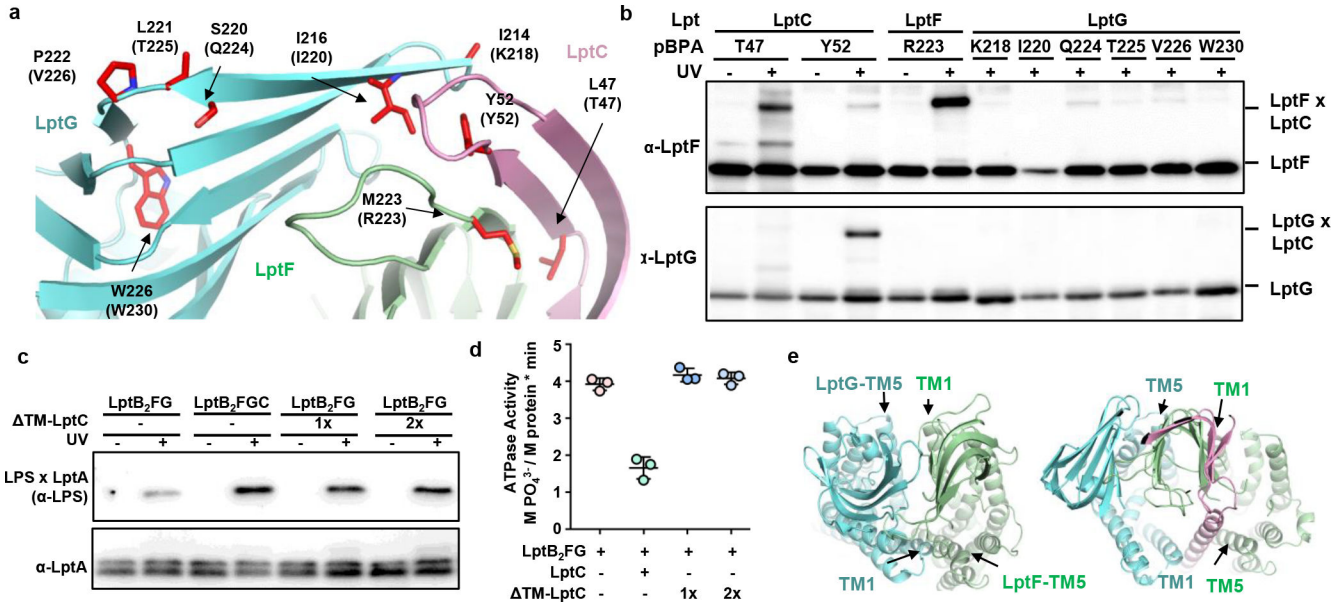

Figure 2: LptC promotes the efficient transport of LPS to LptA.

(**a**) View of the junction between the β-jellyrolls of LptG (blue), LptF (green), and LptC (pink) in the *V. cholerae* $LptB_2FGC$ structure. Amino acids shown as red sticks were substituted with *p*BPA for experiments in panel B; corresponding *E. coli* residues are in parentheses (see Extended Data Fig. 3). (**b**) *E. coli* $LptB_2FGC$ complexes containing *p*BPA were photocrosslinked *in vivo* and adducts were detected by pulling down His-tagged LptC and immunoblotting with antibodies against LptC, LptF, and LptG. Corresponding anti-LptC blots are shown in Extended Data Fig. 4a. (**c**) *E. coli* $LptB_2FG$ or $LptB_2FGC$ complexes were reconstituted into LPS-containing proteoliposomes and their ability to transport LPS to LptA was assessed (see Extended Data Fig. 1b). (**d**) ATP hydrolysis by $LptB_2FG$ or $LptB_2FGC$ in proteoliposomes was monitored by measuring inorganic phosphate levels. Bars represent the averages of three biological replicates, with error bars showing the standard deviation. (**e**) *P. aeruginosa* $LptB_2FG$ structure (left panel, PDB #5×5y;)[20] and *V. cholerae* $LptB_2FGC$ structure (right panel). The *K. pneumoniae* $LptB_2FG$ structure (5l75)[19] is shown in Extended Data Fig. 5a. Blots shown in (b) and (c) are representative of data from 3 biological replicates.

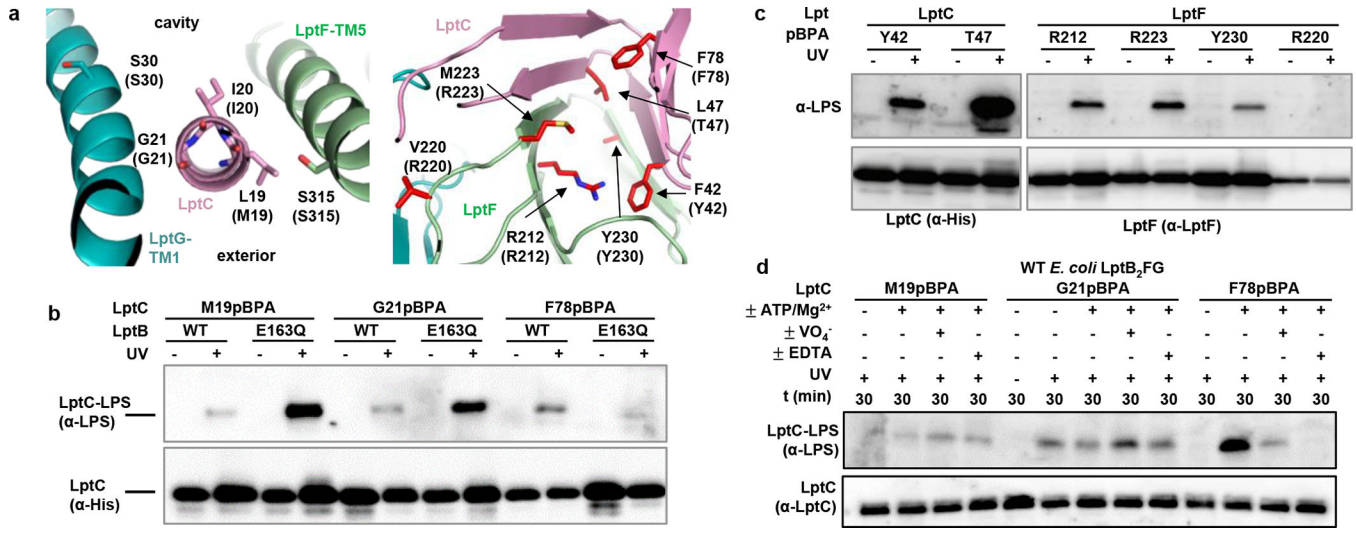

Figure 3: LPS entry into the cavity of the transporter is ATP independent but extraction out of the membrane and onto the bridge requires ATP.

(a) Ribbon diagrams of $LptB_2FGC$ structures showing functionally relevant sites, with LptG colored cyan, LptC pink, and LptF green. Left panel, the gate through which LPS enters the cavity. Right panel, the junction of the β-jellyrolls between *V. cholerae* LptC and LptF. Residues shown as red sticks were substituted with *p*BPA for photocrosslinking experiments (b-d), and the corresponding *E. coli* residues in parentheses. (**b**) *In vivo* photocrosslinking experiments comparing LptC-LPS crosslink strength at three positions in LptC, in $LptB_2FGC$ complexes containing either wild-type LptB or LptB(E163Q), which cannot hydrolyze ATP. Crosslinks to LPS were detected with anti-LPS antibodies. (**c**) In wild-type complexes, residues at the LptC-LptF interface were substituted with *p*BPA and photocrosslinked to LPS *in vivo*. (**d**) *E. coli* $LptB_2FGC$ variants with *p*BPA subsitutions at positions M19, G21, or F78 were reconstituted into proteoliposomes containing LPS. The ability of these LptC variants to crosslink LPS was tested by exposure to UV light after 30 minute incubation with one of no nucleotide (buffer), ATP-Mg^{2+}, ATP-VO_4^-, or ATP-EDTA. See Extended Data Fig. 6 for additional crosslinking experiments that support an external and an internal binding site for LPS at the entry gate, as well as experiments showing undetectable LPS binding to sites in the LptG beta-jellyroll. Data shown in (b), (c), and (d) are representative of results from three biological replicates.

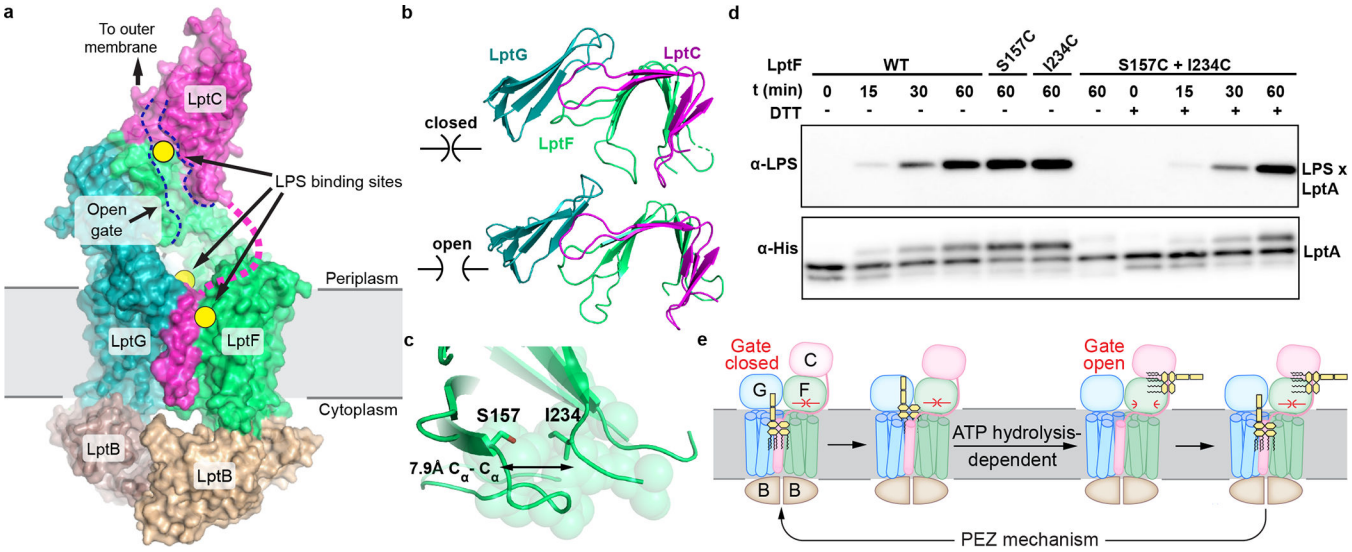

Figure 4: Unidirectional LPS transport is promoted by a gate in the β-jellyroll of LptF.

(**a**) Surface representation of *E. cloacae* $LptB_2FGC$ in a gate-open conformation. Unresolved residues between the TM helix and β-jellyroll of LptC are denoted with a dashed magenta line. The edges of the open surface of the LptF and LptC β-jellyroll domains are highlighted with a dashed blue line. (**b**) The distinct gate-closed and gate-open conformations of the *V. cholerae* complex (top) and the *E. cloacae* complex (bottom) at the LptF-LptC interface. (**c**) Two spatially proximal amino acids in the *V. cholerae* LptF β-jellyroll, S157 and I234, were replaced with cysteines in the corresponding *E. coli* LptF to enforce a closed conformation by spontaneous formation of a disulfide. *V. cholerae* LptF residues 154–157 and 233–236 are shown as semi-transparent spheres to emphasize the close packing of sidechains. (**d**) LPS release to LptA(I36pBPA) from proteoliposomes containing $LptB_2FGC$ with LptF cysteine variants; UV-dependent photocrosslinking to LPS was detected with an anti-LPS antibody, and anti-His blots show the amount of LptA(I36pBPA)-His_6 in each sample. Also see Extended data Figs. 8 and 9. The blots are representative of experiments performed in triplicate. (**e**) Model depicting LPS movement through $LptB_2FGC$ onto the Lpt bridge. The opening and closing of the gate in LptF is denoted by the symbols in panel B.